

A 3D topological insulator quantum dot for optically controlled quantum memory and quantum computing

Hari P. Paudel and Michael N. Leuenberger*

*NanoScience Technology Center and Department of Physics,
University of Central Florida, Orlando, Florida 32826, United States*

We present the model of a quantum dot (QD) consisting of a spherical core-bulk heterostructure made of 3D topological insulator (TI) materials, such as $\text{PbTe}/\text{Pb}_{0.31}\text{Sn}_{0.69}\text{Te}$, with bound massless and helical Weyl states existing at the interface and being confined in all three dimensions. The number of bound states can be controlled by tuning the size of the QD and the magnitude of the core and bulk energy gaps, which determine the confining potential. We demonstrate that such bound Weyl states can be realized for QD sizes of few nanometers. We identify the spin locking and the Kramers pairs, both hallmarks of 3D TIs. In contrast to topologically trivial semiconductor QDs, the confined massless Weyl states in 3D TI QDs are localized at the interface of the QD and exhibit a mirror symmetry in the energy spectrum. We find strict optical selection rules satisfied by both interband and intraband transitions that depend on the polarization of electron-hole pairs and therefore give rise to the Faraday effect due to Pauli exclusion principle. We show that the semi-classical Faraday effect can be used to read out spin quantum memory. When a 3D TI QD is embedded inside a cavity, the single-photon Faraday rotation provides the possibility to implement optically mediated quantum teleportation and quantum information processing with 3D TI QDs, where the qubit is defined by either an electron-hole pair, a single electron spin, or a single hole spin in a 3D TI QD. Remarkably, the combination of inter- and intraband transition gives rise to a large dipole moment of up to 450 Debye. Therefore, the strong-coupling regime can be reached for a cavity quality factor of $Q \approx 10^4$ in the infrared wavelength regime of around $10 \mu\text{m}$.

KEYWORDS: topological insulator, quantum dot, heterostructure.

PACS numbers: 81.07.Ta, 73.40.-c, 78.66.-w, 78.20.Ls

I. INTRODUCTION

3D TIs are narrow-bandgap materials with topologically protected gapless surface/interface states that are characterized by the linear spectrum of massless Weyl fermions.^{1,2} In such materials, the spins of the Kramers pairs are locked at a right angle to their momenta on the Fermi surface due to spin-orbit coupling,³⁻⁹ which can be used for spin current generation.¹⁰⁻¹² The surface states are protected by time reversal symmetry, leading to suppression of backscattering from edges and nonmagnetic impurities.^{1,2,6,13,14} Such states are of great importance in low-power opto-spintronics.^{10,15} Decoherence can be circumvented by highly polarized spin states with helical spin texture,^{3,16-18} leading to a phase coherence length of several hundred nanometers in nanostructures.^{19,20}

In 3D TI nanostructures the special properties of topologically protected surface states of TIs are amplified because of the large surface-to-volume ratio. In addition, the chemical potential can be electrically tuned using a gate voltage. For example, the coherent propagation of the Weyl electrons around the perimeter of a nanoribbon provides excellent evidence of the topological nature of the surface states in TI nanostructures.²⁰ Experiments on both the physical and chemical synthesis of TI nanostructures have been done recently to understand their transport properties at the nanoscale.²¹⁻²³ Recently, in a TI QD with tunable barriers based on ultrathin Bi_2Se_3 films, Coulomb blockade with around 5 meV charging energy was observed.²⁴

So far, a theoretical study of electronic properties of 2D helical states occurring at the nanoscale of 3D TIs, such as in QDs, is still lacking. In this article, we present for the first time the study of bound Weyl states that are confined at the interface of a spherical core-bulk heterostructure QD made of 3D TI materials such as $\text{Pb}_{1-x}\text{Sn}_x\text{Te}$. We show that at the interface massless Weyl fermions are confined in all three dimensions. The directions of spin and momentum are tangent to the surface of the QD. Remarkably, their inherent spin-momentum locking property exists even in a QD. Because of the linear dispersion there is a mirror symmetry in the energy spectrum between positive and negative energy states, in contrast to topologically trivial semiconductors. We demonstrate that this symmetry in energy spectrum is preserved for the QD spectrum.

Several methods have been proposed to implement optically controlled quantum memory and optically mediated quantum computing with topologically trivial QDs. Quantum memories have been recently reviewed in Ref. 25. A recent review on optically controlled quantum computing with electron spins can be found in Ref. 26. Optically controlled single-electron spin memory has been experimentally demonstrated using GaAs QDs²⁷ and InGaAs QDs.²⁸ Exciton memory has been implemented experimentally in a semiconductor nanopost.²⁹ For the purpose of using a hole spin as quantum memory or qubit, high coherence of hole spins in InGaAs QDs has been experimentally shown.³⁰ Ref. 31 demonstrates experimentally that a single spin can be

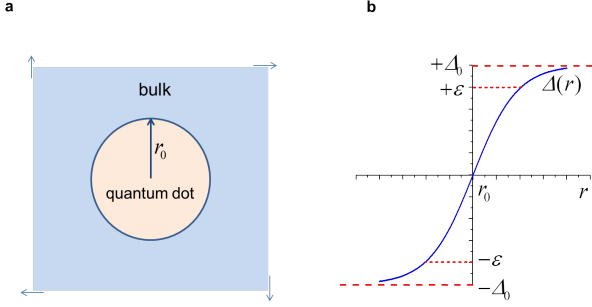


Figure 1: A heterostructure spherical core-bulk 3D TI QD with a single interface. **a.** The arrows indicate the infinite size of the host. The core and bulk host can be chosen as PbTe and $\text{Pb}_{0.31}\text{Sn}_{0.69}\text{Te}$ or vice versa. **b.** The potential $\Delta(r)$ binds Weyl fermions at the interface. The energy of the bound interface states depends on the size of the QD and the strength of the potential. As an example, two bound states at the interface are shown with energies $+\varepsilon$ and $-\varepsilon$ (short dashed lines) for a QD of size $r_0 = 2$ nm.

read out using Faraday rotation. Schemes for optically controlled two-qubit interaction have been proposed that are based on the exchange of virtual photons inside a cavity,³² the optical RKKY interaction,³³ dipole-dipole interaction,³⁴ Substantial experimental progress has been made to implement optically controlled electron spin state preparation,³⁵ hole spin state preparation,³⁶ single-spin readout,³⁷ dephasing protection,³⁸ two-qubit gate,^{39,40} two QD-spin entanglement,⁴¹ and spin-photon entanglement.⁴²

In Refs. 43,44 we developed the method of the Faraday rotation of a single photon due to the Pauli exclusion principle occurring on a topologically trivial QD. Our proposed method can be used for entangling remote excitons, electron spins, and hole spins. We showed that this entanglement can be used for the implementation of optically mediated quantum teleportation and quantum computing. Our ideas and methods have been plagiarized in Ref. 45.

Here we show that classical and single-photon Faraday rotation due to the Pauli exclusion principle in a 3D TI QD occur due to strict optical selection rules satisfied by both interband and intraband transitions that depend on the polarization of electron-hole pairs. Based on this finding we propose that 3D TI QDs can be used as quantum memory and for the implementation of optically mediated quantum teleportation and quantum computing. First, we propose that a single e-h pair in a 3D TI QD can be used as a quantum memory. The information is stored in form of the polarization state of the e-h pair. In order to be able to read out this information multiple times, we develop the method of Faraday rotation of a classical electromagnetic field due to Pauli exclusion principle in a 3D TI QD. Second, we propose that the polarization of a single e-h pair, a single electron spin, or a single hole spin can be used as a qubit in a 3D TI QD for the implemen-

tation of optically mediated quantum teleportation and quantum computing. We develop the method of single-photon Faraday rotation in a 3D TI QD, which creates the entanglement between a single photon and a qubit on the 3D TI QD. This entanglement is the resource for the implementation of quantum teleportation and quantum computing.

In wide bandgap semiconductor QDs optical inter- and intraband transitions are energetically separated because the bandgap is typically much larger than the QD level spacing.⁴⁶ In contrast to that, we show that in 3D TI QDs inter- and intraband transitions combine because of the vanishing bandgap at band crossing. The resulting large dipole moment of up to 450 Debye provides the possibility to reach the strong-coupling regime for a cavity quality factor of $Q \approx 10^4$ in the infrared wavelength regime of around 10 μm .

The paper is organized as follows. In Sec. II we present the analytical derivation of the Weyl solution of the radial Dirac equation using Greens function technique at the bulk-quantum dot interface. The resulting eigenvalues and eigenfunctions are analyzed in the Sec. III. The Sec. IV is devoted to the evaluation of the optical transition matrix elements and the discussion on them. We also discuss on the potential applications of our results. In Sec. V we explain the Faraday rotation effect achieve in the 3D TI QD. The application of the 3D TI QD as a quantum memory is explained in the Sec. VI. where we also explain the Stark energy shift that can be used to achieve clean selection rules for the excitation of a single electron-hole (e-h) pair. The Sec. VII and VIII are devoted to the detailed description of the single-photon Faraday effect, where we show that a single e-h pair, a single electron, or a single hole can be used as a qubit to implement optically mediated quantum teleportation and quantum computing with 3D TI QDs. In this section, different possible level configurations of the Weyl states are shown to achieve the Faraday rotation effect.

II. MODEL BASED ON DIRAC EQUATION

In Fig. 1 we show the model of our spherically symmetric 3D TI QD of a core-bulk structure with a single interface at radius $r = r_0$. This core-bulk structure consists, for example, of an inner core of PbTe and an outer bulk of $\text{Pb}_{0.31}\text{Sn}_{0.69}\text{Te}$ with bandgaps of 0.187 and -0.187 eV, respectively, or vice versa, so that Weyl fermions are generated at the interface. Here we used the bandgap formula provided in Ref. 24 for determining x . Note that the band crossing happens in $\text{Pb}_{1-x}\text{Sn}_x\text{Te}$ at $x = 0.35$ at 4 K. The Weyl fermions are subjected to the spherically symmetric potential $\Delta(r)$ (Fig. 1 (b)).

To understand the properties of a 3D TI QD, we start with the Dirac Hamiltonian within the $\mathbf{k} \cdot \mathbf{p}$ approximation.⁴⁷ Neglecting the far band terms, we have

$$H = v_{\parallel} \alpha_z \hat{p}_z + v_{\perp} \boldsymbol{\alpha}_{\perp} \cdot \hat{\mathbf{p}} + \beta \Delta \quad (1)$$

where $\alpha = \begin{pmatrix} 0 & \sigma \\ \sigma & 0 \end{pmatrix}$ are the Dirac α -matrices, σ are the Pauli matrices, $\beta = \begin{pmatrix} 1 & 0 \\ 0 & -1 \end{pmatrix}$ is the Dirac β -matrix, and $\hat{\mathbf{p}}$ is the momentum operator. The component of the Fermi velocities v_\perp and v_\parallel in angular and radial direction are determined by the $v_\perp = P_\perp/m_0$ and $v_\parallel = P_\parallel/m_0$ respectively, where P_\perp and P_\parallel are the interband matrix elements. $m_0 = 9.10938188 \times 10^{-31}$ kg is the free electron mass. $\Delta(\mathbf{r}) = \varepsilon_g(\mathbf{r})/2$ is the gap energy parameter.

Assuming spherical symmetry for the 3D TI QD, $\Delta(r)$ depends on the radial coordinate only which breaks the crystal symmetry in radial direction and has the symmetry $\Delta(r - r_0) = -\Delta(r_0 - r)$, where r_0 is the radius of the QD. Therefore, the angular parts are separated from the radial part of the Dirac Hamiltonian (1). Thus, we can follow the derivation of the solution for the central-force problem of a hydrogen atom in relativistic quantum mechanics.⁴⁸ The eigenfunctions of H are four-component spinors $\Phi = \begin{bmatrix} \phi_- \\ \phi_+ \end{bmatrix} = \begin{bmatrix} f_-(r) \mathcal{Y}_{j l_-}^{m_j} \\ i f_+(r) \mathcal{Y}_{j l_+}^{m_j} \end{bmatrix}$, where f_- and f_+ are the radial functions and $\mathcal{Y}_{j l_-}^{m_j}$ and $\mathcal{Y}_{j l_+}^{m_j}$ are the normalized spin-angular functions corresponding to the L_- and L_+ band, respectively, such as in $\text{Pb}_{1-x}\text{Sn}_x\text{Te}$. After eliminating the angular parts, the radial part of the Dirac Hamiltonian (1) takes the form

$$H = \begin{pmatrix} \Delta(r) & -v_\parallel \hbar \left(\frac{d}{dr} - \frac{\kappa}{r} \right) \\ v_\parallel \hbar \left(\frac{d}{dr} + \frac{\kappa}{r} \right) & -\Delta(r) \end{pmatrix} \quad (2)$$

where $v_\parallel = 2.24 \times 10^5$ m/s for $\text{Pb}_{1-x}\text{Sn}_x\text{Te}$ and $\kappa = \pm(j + \frac{1}{2})$ is a nonzero positive or negative integer, j being the total angular momentum quantum number. For given κ , it is known from relativistic quantum mechanics that the angular momenta l_- and l_+ for ϕ_- and ϕ_+ are determined by the relations $-\kappa = j(j+1) - l_-(l_-+1) + 1/4$ and $\kappa = j(j+1) - l_+(l_++1) + 1/4$, respectively. By solving $H^2\Phi = \varepsilon^2\Phi$, we obtain

$$\left(r^2 \frac{d^2}{dr^2} + 2r \frac{d}{dr} \right) F_\mp - (\lambda^2 r^2 + \kappa(\kappa \pm 1)) F_\mp = \beta r^2 \frac{d\Delta}{dr} F_\pm \quad (3)$$

where $F_\pm = r f_\pm$, $\beta = 1/v_\parallel \hbar$ and $\lambda = \beta \sqrt{(\Delta_0^2 - \varepsilon^2)}$. λ behaves like a wave vector \mathbf{k} whose allowed quantized values determine the particle's energy levels. In a flat geometry of a thin layer of a 3D TI, $\Delta(z)$ can be chosen to be $\Delta(z) = \Delta(\infty) \tanh(z/l)$.^{49,50} We adopt a similar potential along the radial direction of the form $\Delta(r') = \Delta_0 \text{sgn}(r' - r_0)$. Hence, the source term in Eq. (3) is $\mathcal{F}_\pm(r') = 2\Delta_0 \beta F_\pm(r_0) r'^2 \delta(r' - r_0)$. Eqs. (3) can be solved by using the corresponding differential equation for the Green's function, i.e.

$$\left[\frac{d}{dr} \left(r^2 \frac{d}{dr} \right) - (\lambda^2 r^2 + \kappa(\kappa \pm 1)) \right] G_\mp = \delta(r - r') \quad (4)$$

The solutions regular at $r = 0$ with outgoing wave behavior at $r \rightarrow \infty$ are the product of spherical modified

Bessel functions of the order κ for G_- and of the order $\kappa - 1$ for G_+ , i.e. $G_- (r, r', \lambda) = C_- \mathcal{I}_\kappa(\lambda r_<) \mathcal{K}_\kappa(\lambda r_>)$, $G_+ (r, r', \lambda) = C_+ \mathcal{I}_{\kappa-1}(\lambda r_<) \mathcal{K}_{\kappa-1}(\lambda r_>)$, where $r_< (r_>)$ is the smaller (larger) of r and r' . The functions $\mathcal{I}(\lambda r)$ and $\mathcal{K}(\lambda r)$ are, respectively, the first and the second kind of modified spherical Bessel functions, and C_\mp are the normalization constants. These constants are determined by the discontinuity in slope implied by the delta function in Eq. (4). Integration is performed at the interface of the QD along the radial direction:

$\left[r^2 \frac{dG_\mp}{dr} \right]_{r'-\eta}^{r'+\eta} = 1$, where η is an infinitesimal quantity with $\eta > 0$. For $r = r' + \eta$, $r_> = r$, $r_< = r'$ and for $r = r' - \eta$, $r_> = r'$, $r_< = r$. Consequently, the normalization constants are $C_- = 1/\lambda r_0'^2 W_\kappa$ and $C_+ = 1/\lambda r_0'^2 W_{\kappa-1}$, where $W_\kappa = [\mathcal{I}_\kappa(\lambda r') \mathcal{K}'_\kappa(\lambda r) - \mathcal{I}'_\kappa(\lambda r) \mathcal{K}_\kappa(\lambda r')]_{r=r'}$ and $W_{\kappa-1} = [\mathcal{I}_{\kappa-1}(\lambda r') \mathcal{K}'_{\kappa-1}(\lambda r) - \mathcal{I}'_{\kappa-1}(\lambda r) \mathcal{K}_{\kappa-1}(\lambda r')]_{r=r'}$ are the Wronskians of $\mathcal{I}(\lambda r)$ and $\mathcal{K}(\lambda r)$, respectively, for κ and $\kappa - 1$ order, and $\mathcal{I}'(\lambda r)$ and $\mathcal{K}'(\lambda r)$ are derivatives of the Bessel functions. The Wronskian of two linearly independent functions is proportional to $1/r^2$ for Sturm-Liouville type equations such as Eq. (4) (see the App. A). The solutions of Eqs. (3) are $F_\mp = \int G_\mp(r, r', \lambda) \mathcal{F}_\pm(r') dr' = 2\Delta_0 \beta \int G_\mp(r, r', \lambda) F_\pm(r_0) r'^2 \delta(r' - r_0) dr'$, i.e.

$$F_-(r) = 2\Delta_0 \beta F_+(r_0) \mathcal{I}_\kappa(\lambda r_<) \mathcal{K}_\kappa(\lambda r_>) / \lambda W_\kappa \quad (5)$$

$$F_+(r) = 2\Delta_0 \beta F_-(r_0) \mathcal{I}_{\kappa-1}(\lambda r_<) \mathcal{K}_{\kappa-1}(\lambda r_>) / \lambda W_{\kappa-1} \quad (6)$$

where $r_< (r_>)$ is now the smaller (larger) of r and r_0 . A transcendental equation is obtained by solving Eqs. (5) and (6) and evaluating at $r = r_0$,

$$[z \mathcal{I}_\kappa(z) \mathcal{K}_\kappa(z)] [z \mathcal{I}_{\kappa-1}(z) \mathcal{K}_{\kappa-1}(z)] = 1/4 \Delta_0^2 \beta^2 r_0^2 \quad (7)$$

where $z = \lambda r_0$. In Fig. 2, we show the plot of Eq. (7) where the function $F(z)$ is defined as $F(z) = [z \mathcal{I}_\kappa(z) \mathcal{K}_\kappa(z)] [z \mathcal{I}_{\kappa-1}(z) \mathcal{K}_{\kappa-1}(z)]$.

III. BOUND STATES OF THE WEYL FERMIONS

Each term in the square bracket on the left hand side of Eq. (7) is a monotonically decreasing function of z (for $z > 0$), with maximum value of $1/(2\kappa + 1)$ for κ^{th} order term and $1/(2\kappa - 1)$ for $(\kappa - 1)^{th}$ order term occurring at $z = 0$ (see the App. B). Therefore, their product has a maximum value of $1/(4\kappa^2 - 1)$ at $z = 0$ and is equal to $1/4 \Delta_0^2 \beta^2 r_0^2$. Since $F(z)$ is a monotonically decreasing function, for each κ , there is at most a single solution given by the intersection of $F(z)$ with the constant $1/4 \Delta_0^2 \beta^2 r_0^2$ (dashed line and solid line in Fig.

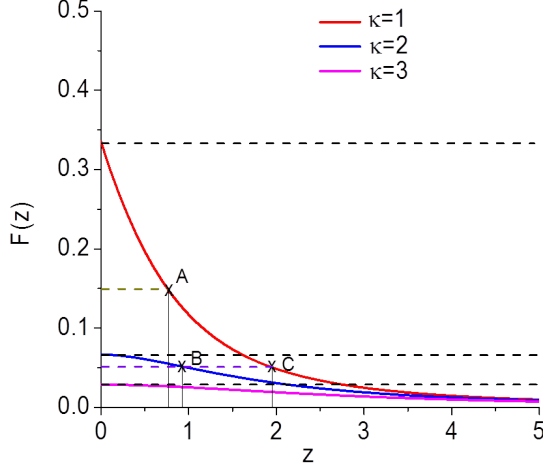


Figure 2: Plot of Eq. (7) showing the intersections of the monotonically decreasing $F(z)$ (solid lines) with the constants (black dashed lines). Intersection at $z = 0$ gives the minimum threshold of the size of a QD to have two bound states, one positive and one negative energy state, for a given confining potential. For a larger QD, multiple bound states exist, corresponding to multiple intersection points. The intersection points A, B and C are example points where we evaluate the wavefunctions. The energy of the bound states are determined by the relation $z = \lambda r_o$.

2). The critical limit for having a single solution is determined by the intersection at the maximum value of $F(z)$, which occurs at $z = 0$. This means that there exists a single solution of Eq. (7) for each κ as long as the condition $1/4\Delta_o^2\beta^2r_o^2 \leq 1/(4\kappa^2 - 1)$ is satisfied. Fig. 2 shows the plot of the first three different values of κ , $\kappa = 1$ (red), 2 (blue) and 3 (pink), each a monotonically decreasing line (solid line) cut by a horizontal line (dashed line) at most one time. Since $\lambda = \beta\sqrt{(\Delta_o^2 - \varepsilon^2)}$, each single solution gives rise to two bound states with same magnitude but opposite sign of energy, giving rise to the mirror symmetry in the energy spectrum. Indeed, this makes sense since Weyl fermions are massless at zero band gap with the linear dispersion relation. Note that there is no radial quantum number because in general a Dirac potential allows only for a single positive-energy and a single negative-energy solution in radial direction.

As the size of the QD grows, it is filled with more and more bound states (see Fig. 2) where for smaller value of $F(z)$, a horizontal dashed line makes multiple cuts at different values of the energy (i.e. z) for different κ . For negative κ , the solutions diverge at the origin and are therefore physically not valid. This result has profound implications because the sign of κ determines whether \mathbf{j} is parallel or antiparallel to the spin \mathbf{s} (see Ref. 26). Since κ is only allowed to be positive, only one spin orientation with respect to \mathbf{j} is permitted. This corresponds to the spin locking effect, which is a hallmark of 3D TIs. This

ϕ_-			ϕ_+		
κ	l_-	j	κ	l_+	j
1	1	1/2	1	0	1/2
2	2	3/2	2	1	3/2
3	3	5/2	3	2	5/2
4	4	7/2	4	3	7/2

Table I: ϕ_- and ϕ_+ components

allows us to write down the more specific form of the spin-angular functions, i.e.

$$\mathcal{Y}_{jl_-}^{m_j} = -\sqrt{\frac{l_- - m_j + \frac{1}{2}}{2l_- + 1}} Y_{l_-}^{m_j - \frac{1}{2}} \begin{bmatrix} 1 \\ 0 \end{bmatrix} + \sqrt{\frac{l_- + m_j + \frac{1}{2}}{2l_- + 1}} Y_{l_-}^{m_j + \frac{1}{2}} \begin{bmatrix} 0 \\ 1 \end{bmatrix} \quad (8)$$

$$\mathcal{Y}_{jl_+}^{m_j} = \sqrt{\frac{l_+ + m_j + \frac{1}{2}}{2l_+ + 1}} Y_{l_+}^{m_j - \frac{1}{2}} \begin{bmatrix} 1 \\ 0 \end{bmatrix} + \sqrt{\frac{l_+ - m_j + \frac{1}{2}}{2l_+ + 1}} Y_{l_+}^{m_j + \frac{1}{2}} \begin{bmatrix} 0 \\ 1 \end{bmatrix} \quad (9)$$

where $l_- = j + \frac{1}{2}$ and $l_+ = j - \frac{1}{2}$.

The condition $1/4\Delta_o^2\beta^2r_o^2 = 1/(4\kappa^2 - 1)$ determines the lower limit of the size of the QD to hold two bound interface states, a positive and a negative energy state, for a given value of the confining potential strength. The critical QD size depends on the Fermi velocities and band gaps of the 3D TI materials. In $\text{Pb}_{1-x}\text{Sn}_x\text{Te}$, $\Delta_o = 0.0935$ eV, half of the band gap of PbTe. Choosing $v_{\parallel} = 2.24 \times 10^5$ m/s,⁵⁰ results in a critical QD size of $r_o = 1.4$ nm for $\kappa = 1$ at $z = 0$. Similarly for $\kappa = 2$ at $z = 0$, the critical QD size for $\text{Pb}_{1-x}\text{Sn}_x\text{Te}$ is $r_o = 3$ nm. The energy of the bound states are determined from $z = \lambda r_o$, which gives a very shallow energy level of $\varepsilon = \pm\Delta_o$ for $z = 0$.

For a given value of κ , quantum numbers characterizing the wavefunctions ϕ_- and ϕ_+ can be determined. For $\kappa = 1, 2, 3$ and 4, the possible combination of the quantum numbers are shown in Table I for both spinors ϕ_- and ϕ_+ . Here we observe that the ϕ_- component is characterized by the spin being antiparallel to its angular momentum, whereas the ϕ_+ component is characterized by the spin being parallel to its angular momentum. We show now how to identify the Kramers pairs. According to Kramers theorem, which applies to a time-reversal invariant system, a spin 1/2 state is at least twofold degenerate on the surface of a 3D TI. Hence, we obtain the following examples of Kramers pairs. For $\kappa = 1$, the

4-spinor state with $m_{\frac{1}{2}} = \frac{1}{2}$,

$$\begin{aligned} \Phi_{\frac{1}{2}, \frac{1}{2}}^{\kappa=1} &= \begin{bmatrix} f_{-}(r) \mathcal{Y}_{\frac{1}{2}, \frac{1}{2}}^{\frac{1}{2}} \\ i f_{+}(r) \mathcal{Y}_{\frac{1}{2}, \frac{1}{2}}^{\frac{1}{2}} \end{bmatrix} \\ &= \begin{bmatrix} f_{-}(r) \left(-\sqrt{\frac{1}{3}} Y_1^0 \begin{bmatrix} 1 \\ 0 \end{bmatrix} + \sqrt{\frac{2}{3}} Y_1^1 \begin{bmatrix} 0 \\ 1 \end{bmatrix} \right) \\ i f_{+}(r) Y_0^0 \begin{bmatrix} 1 \\ 0 \end{bmatrix} \end{bmatrix} \end{aligned} \quad (10)$$

has as Kramers partner the 4-spinor state with $m_{\frac{1}{2}} = -\frac{1}{2}$,

$$\begin{aligned} \Phi_{\frac{1}{2}, -\frac{1}{2}}^{\kappa=1} &= \begin{bmatrix} f_{-}(r) \mathcal{Y}_{\frac{1}{2}, -\frac{1}{2}}^{-\frac{1}{2}} \\ i f_{+}(r) \mathcal{Y}_{\frac{1}{2}, -\frac{1}{2}}^{-\frac{1}{2}} \end{bmatrix} \\ &= \begin{bmatrix} f_{-}(r) \left(-\sqrt{\frac{2}{3}} Y_1^{-1} \begin{bmatrix} 1 \\ 0 \end{bmatrix} + \sqrt{\frac{1}{3}} Y_1^0 \begin{bmatrix} 0 \\ 1 \end{bmatrix} \right) \\ i f_{+}(r) Y_0^0 \begin{bmatrix} 0 \\ 1 \end{bmatrix} \end{bmatrix} \end{aligned} \quad (11)$$

For $\kappa = 2$, the 4-spinor state with $m_{\frac{3}{2}} = \frac{3}{2}$,

$$\begin{aligned} \Phi_{\frac{3}{2}, \frac{3}{2}}^{\kappa=2} &= \begin{bmatrix} f_{-}(r) \mathcal{Y}_{\frac{3}{2}, \frac{3}{2}}^{\frac{3}{2}} \\ i f_{+}(r) \mathcal{Y}_{\frac{3}{2}, \frac{3}{2}}^{\frac{3}{2}} \end{bmatrix} \\ &= \begin{bmatrix} f_{-}(r) \left(-\sqrt{\frac{1}{5}} Y_2^1 \begin{bmatrix} 1 \\ 0 \end{bmatrix} + \sqrt{\frac{4}{5}} Y_2^2 \begin{bmatrix} 0 \\ 1 \end{bmatrix} \right) \\ i f_{+}(r) Y_1^1 \begin{bmatrix} 1 \\ 0 \end{bmatrix} \end{bmatrix} \end{aligned} \quad (12)$$

has as Kramers partner the 4-spinor with $m_{\frac{3}{2}} = -\frac{3}{2}$,

$$\begin{aligned} \Phi_{\frac{3}{2}, -\frac{3}{2}}^{\kappa=2} &= \begin{bmatrix} f_{-}(r) \mathcal{Y}_{\frac{3}{2}, -\frac{3}{2}}^{-\frac{3}{2}} \\ i f_{+}(r) \mathcal{Y}_{\frac{3}{2}, -\frac{3}{2}}^{-\frac{3}{2}} \end{bmatrix} \\ &= \begin{bmatrix} f_{-}(r) \left(-\sqrt{\frac{4}{5}} Y_2^{-2} \begin{bmatrix} 1 \\ 0 \end{bmatrix} + \sqrt{\frac{1}{5}} Y_2^{-1} \begin{bmatrix} 0 \\ 1 \end{bmatrix} \right) \\ i f_{+}(r) Y_1^{-1} \begin{bmatrix} 0 \\ 1 \end{bmatrix} \end{bmatrix} \end{aligned} \quad (13)$$

For $\kappa = 2$, the 4-spinor state with $m_{\frac{3}{2}} = \frac{1}{2}$,

$$\begin{aligned} \Phi_{\frac{3}{2}, \frac{1}{2}}^{\kappa=2} &= \begin{bmatrix} f_{-}(r) \mathcal{Y}_{\frac{3}{2}, \frac{1}{2}}^{\frac{1}{2}} \\ i f_{+}(r) \mathcal{Y}_{\frac{3}{2}, \frac{1}{2}}^{\frac{1}{2}} \end{bmatrix} \\ &= \begin{bmatrix} f_{-}(r) \left(-\sqrt{\frac{2}{5}} Y_2^0 \begin{bmatrix} 1 \\ 0 \end{bmatrix} + \sqrt{\frac{3}{5}} Y_2^1 \begin{bmatrix} 0 \\ 1 \end{bmatrix} \right) \\ i f_{+}(r) \left(\sqrt{\frac{2}{3}} Y_1^0 \begin{bmatrix} 1 \\ 0 \end{bmatrix} + \sqrt{\frac{1}{3}} Y_1^1 \begin{bmatrix} 0 \\ 1 \end{bmatrix} \right) \end{bmatrix} \end{aligned} \quad (14)$$

calculated for the intersection point A (ref. Figure 2)

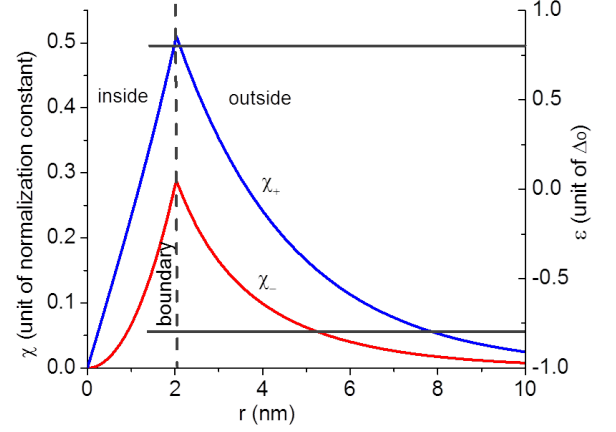


Figure 3: Spatial dependence of f_{-} and f_{+} inside and outside the QD calculated for the intersection point A shown in Fig. 2. The QD has size $r_0 = 2$ nm. The solid horizontal lines represent the energy eigenvalues $\varepsilon_{\pm} = \pm 0.8 \Delta_o$.

has as Kramers partner the 4-spinor with $m_{\frac{3}{2}} = -\frac{1}{2}$,

$$\begin{aligned} \Phi_{\frac{3}{2}, -\frac{1}{2}}^{\kappa=2} &= \begin{bmatrix} f_{-}(r) \mathcal{Y}_{\frac{3}{2}, -\frac{1}{2}}^{-\frac{1}{2}} \\ i f_{+}(r) \mathcal{Y}_{\frac{3}{2}, -\frac{1}{2}}^{-\frac{1}{2}} \end{bmatrix} \\ &= \begin{bmatrix} f_{-}(r) \left(-\sqrt{\frac{3}{5}} Y_2^{-1} \begin{bmatrix} 1 \\ 0 \end{bmatrix} + \sqrt{\frac{2}{5}} Y_2^0 \begin{bmatrix} 0 \\ 1 \end{bmatrix} \right) \\ i f_{+}(r) \left(\sqrt{\frac{1}{3}} Y_1^{-1} \begin{bmatrix} 1 \\ 0 \end{bmatrix} + \sqrt{\frac{2}{3}} Y_1^0 \begin{bmatrix} 0 \\ 1 \end{bmatrix} \right) \end{bmatrix} \end{aligned} \quad (15)$$

In general, the number of Kramers pairs is determined by the spin multiplicity for each m_j value.

In Figs. 3 and 4 we show the spatial wavefunctions of the f_{-} and f_{+} components inside and outside the QD made of the core-bulk heterostructure PbTe/Pb_{0.31}Sn_{0.69}Te. The Fig. 3 shows the example of the intersection point A (see Fig. 2) and the Fig. 4 shows the example of the intersection points B and C (see Fig. 2). Since the 4-spinors must be continuous at the boundary, also each of the 2-spinor components must be continuous, i.e. $f_{-}^{in} = f_{-}^{out}$ and $f_{+}^{in} = f_{+}^{out}$ at the QD surface. The horizontal solid and short dashed lines in Figs. represent the energy eigenvalues, respectively, at the intersection point A, corresponding to $r_0 = 2$ nm, and at the intersection point B and C, corresponding to $r_0 = 3.5$ nm. Eigenvalues are $\varepsilon_{\pm} = \pm 0.80 \Delta_o$ at point A, $\varepsilon_{\pm} = \pm 0.91 \Delta_o$ at point B, and $\varepsilon_{\pm} = \pm 0.48 \Delta_o$ at point C.

In order to show that the solutions correspond to Weyl fermions, we perform an expansion of Eq. (7) for large z to obtain the eigenenergies in the continuum limit. Using the second order in the expansion of the spherical modified Bessel functions for $z \rightarrow \infty$ (see the App. B), we get

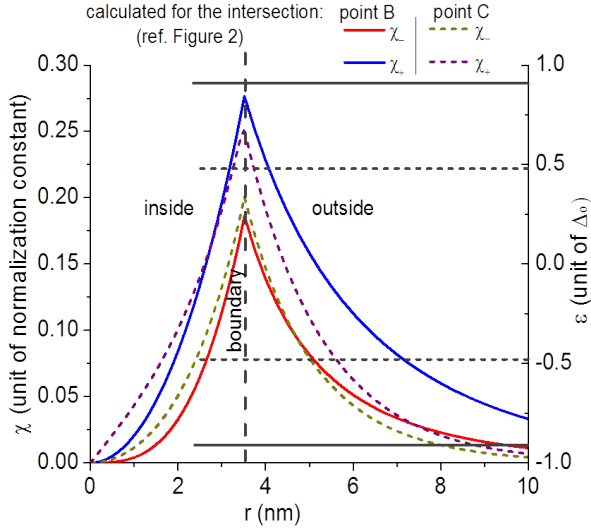


Figure 4: Spatial dependence of f_- and f_+ inside and outside the QD calculated for the intersection points B and C shown in Fig. 2. The QD has size $r_0 = 3.5$ nm. The horizontal solid lines represent the energy eigenvalues $\varepsilon_{\pm} = \pm 0.91\Delta_o$ at point B and the dotted lines represents the energy eigenvalues $\varepsilon_{\pm} = \pm 0.48\Delta_o$ at point C.

$$\frac{1}{2z} \left[1 - \frac{2\kappa(\kappa+1)}{(2z)^2} \right] \times \frac{1}{2z} \left[1 - \frac{2\kappa(\kappa-1)}{(2z)^2} \right] = 1/4\Delta_o^2\beta^2r_o^2. \quad (16)$$

This can be written as

$$\varepsilon^4 - \varepsilon^2\Delta_o^2 + \frac{\Delta_o^2\kappa^2}{\beta^2r_o^2} = 0 \quad (17)$$

which results in the eigenenergies for the electron and hole,

$$\varepsilon_{\pm} = \pm \kappa v_{||} \hbar / r_o. \quad (18)$$

This corresponds to the linear spectrum of free massless Dirac fermions, i.e. free Weyl fermions on a sphere. This means that the energy splittings between the trapped Weyl states in the quantum dot result from the confinement of the Weyl fermions on a sphere. The solution in Eq. (18) corresponds to the eigenspectra found in Ref. 51 for zero magnetic field and without quantum confinement effects.

In the continuum limit, the Nielsen-Ninomiya fermion doubling theorem⁵² is satisfied by the pairs of Dirac cones positioned at antipodal points of the sphere defined by the surface of the QD (see App. C for details). However, for a general finite QD radius r_o the eigenstates are bound and have a discrete energy spectrum. Since the Nielsen-Ninomiya fermion doubling theorem⁵² is valid only for continuum states, it does not apply to the bound Weyl fermions in a 3D TI QD with finite radius r_o .

IV. OPTICAL EXCITATIONS

The $\mathbf{k} \cdot \mathbf{p}$ Hamiltonian contains also a quadratic term in the momenta,⁴⁷ namely

$$H_q = \begin{pmatrix} \frac{(p_z + eA_z)^2}{2m_{||}^-} + \frac{(\mathbf{p}_{\perp} + e\mathbf{A}_{\perp})^2}{2m_{\perp}^-} & 0 \\ 0 & \frac{(p_z + eA_z)^2}{2m_{||}^+} + \frac{(\mathbf{p}_{\perp} + e\mathbf{A}_{\perp})^2}{2m_{\perp}^+} \end{pmatrix}, \quad (19)$$

where $m_{||}^{\mp}$ and m_{\perp}^{\mp} are the longitudinal and transverse effective masses of the L^{\mp} bands, respectively. Through minimal coupling the quadratic term leads to a linear term in the momentum, which we need to take into account. Hence, in the presence of electromagnetic radiation, the total Hamiltonian for the Dirac particle is given by

$$\begin{aligned} H_{\text{tot}} &= v_{||}\alpha_z(\hat{p}_z + eA_z) + v_{\perp}\boldsymbol{\alpha}_{\perp} \cdot (\hat{\mathbf{p}} + e\mathbf{A}_{\perp}) + \beta\Delta - e\hat{\mathbf{r}} \cdot \mathbf{E} \\ &= \begin{pmatrix} \Delta - e\hat{\mathbf{r}} \cdot \mathbf{E} & v_{||}\sigma_z(\hat{p}_z + eA_z) + v_{\perp}\boldsymbol{\sigma}_{\perp} \cdot (\hat{\mathbf{p}} + e\mathbf{A}_{\perp}) \\ v_{||}\sigma_z(\hat{p}_z + eA_z) + v_{\perp}\boldsymbol{\sigma}_{\perp} \cdot (\hat{\mathbf{p}} + e\mathbf{A}_{\perp}) & -\Delta - e\hat{\mathbf{r}} \cdot \mathbf{E} \end{pmatrix}. \end{aligned} \quad (20)$$

where $\mathbf{A} = (A_z, \mathbf{A}_{\perp})$ is the vector potential, $\mathbf{E} = \partial\mathbf{A}/\partial t$ in the Coulomb gauge, and we made use of the equivalence between $(e/m)\mathbf{A} \cdot \mathbf{p}$ and $-e\hat{\mathbf{r}} \cdot \mathbf{E}$.⁴⁸ We identify the

interaction Hamiltonian as

$$\begin{aligned} H_{\text{int}} &= ev_{||}\alpha_z A_z + ev_{\perp}\boldsymbol{\alpha}_{\perp} \cdot \mathbf{A}_{\perp} - e\hat{\mathbf{r}} \cdot \mathbf{E} \\ &= \begin{pmatrix} -e\hat{\mathbf{r}} \cdot \mathbf{E} & ev_{||}\sigma_z A_z + ev_{\perp}\boldsymbol{\sigma}_{\perp} \cdot \mathbf{A}_{\perp} \\ ev_{||}\sigma_z A_z + ev_{\perp}\boldsymbol{\sigma}_{\perp} \cdot \mathbf{A}_{\perp} & -e\hat{\mathbf{r}} \cdot \mathbf{E} \end{pmatrix}. \end{aligned} \quad (21)$$

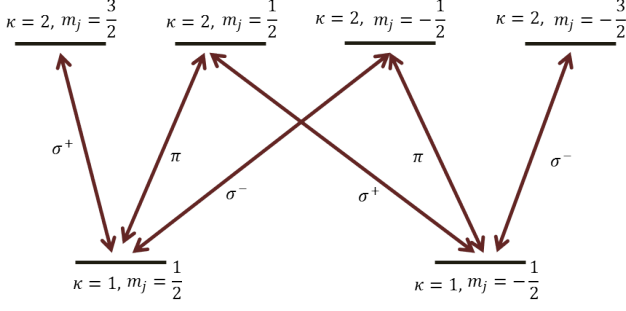


Figure 5: Optical transitions between the states $\kappa = 1$ and $\kappa = 2$ in 3D TI QD. Transitions are vertical. The transitions between $|\Phi_{\frac{1}{2}, \pm \frac{1}{2}}^{\kappa=1}\rangle$ and $|\Phi_{\frac{3}{2}, \pm \frac{1}{2}}^{\kappa=2}\rangle$ are coupled to the linear polarization of the incoming photons, while the transitions between $|\Phi_{\frac{1}{2}, \pm \frac{1}{2}}^{\kappa=1}\rangle$ and $|\Phi_{\frac{3}{2}, \mp \frac{1}{2}}^{\kappa=2}\rangle$ and the transitions between $|\Phi_{\frac{1}{2}, \pm \frac{1}{2}}^{\kappa=1}\rangle$ and $|\Phi_{\frac{3}{2}, \pm \frac{3}{2}}^{\kappa=2}\rangle$ are coupled to the right and left circularly polarized light, respectively.

It will turn out that both interband and intraband transitions contribute. It is important to note that $v_{\parallel} = P_{\parallel}/m_0$ and $v_{\perp} = P_{\perp}/m_0$ include the Kane interband matrix elements $\mathbf{P} = \langle u_{\mathbf{k}_f}^{\mp} | \hat{\mathbf{p}} | u_{\mathbf{k}_i}^{\pm} \rangle$, where $u_{\mathbf{k}}^{\mp}$ are the Bloch's functions for the L^{\mp} bands. This means that the interband transitions are governed by the interband Hamiltonian $H_{inter} = ev_{\parallel} \alpha_z A_z + ev_{\perp} \alpha_{\perp} \cdot \mathbf{A}_{\perp}$, where the Dirac α -matrices couple the L^- band with the L^+ band. The Hamiltonian $H_{intra} = -e\hat{\mathbf{r}} \cdot \mathbf{E}$ accounts for intraband transitions with $\hat{\mathbf{r}}$ operating on the envelope wavefunctions only. H_{intra} is proportional to the identity in 4-spinor space and therefore couples the L^- band to itself and the L^+ band to itself. Thus the interband Hamiltonian H_{inter} and the intraband Hamiltonian H_{intra} are not equivalent in this description. On the one hand, H_{inter} gives rise to interband transitions because it contains the Kane interband matrix elements P_{\perp} and P_{\parallel} . On the other hand, H_{intra} gives rise to intraband transitions because the electric dipole operator $e\hat{\mathbf{r}}$ operates on the envelope wavefunctions. Remarkably, both terms lead to the same strict optical selection rules and add up to a combined optical matrix element, as shown below. This enhancement of the optical matrix element is a feature of the 3D TI QD. In contrast, in a wide-bandgap semiconductor QD the interband and intraband transitions are energetically separated, i.e. interband transitions occur typically around the bandgap energy, whereas intraband transitions occur around the energy level separation due to the confinement of the QD.⁴⁶

Fig. 5 shows the possible transitions between the states $\kappa = 1$ and $\kappa = 2$. It is to be noted that there is a complete symmetry in the solutions in the sense that a κ state can be chosen from either the positive- or the negative-energy solutions.. The optical matrix elements are given by

$$\begin{aligned} \langle \phi_f | H_{int} | \phi_I \rangle = & ev_{\parallel} \langle \phi_f | \alpha_z | \phi_I \rangle A_z \\ & + ev_{\perp} \langle \phi_f | \alpha_{\perp} | \phi_I \rangle \cdot \mathbf{A}_{\perp} \\ & - e \langle \phi_f | \hat{\mathbf{r}} | \phi_I \rangle \cdot \mathbf{E} \end{aligned} \quad (22)$$

The incoming photon's wavelength is much larger than the dot size. Therefore, the transitions are vertical, which means $\mathbf{A} = (A_{x0}, A_{y0}, A_{z0})e^{i\mathbf{q} \cdot \mathbf{r}} \approx (A_{x0}, A_{y0}, A_{z0})$ can be used, yielding the electric dipole approximation. The transition energies $\hbar\omega_0 = \varepsilon_{\kappa=2} - \varepsilon_{\kappa=1}$ are large compared with the room temperature $k_B T = 25$ meV and the Coulomb charging energy of about 5 meV.²⁴ For the control of the number of electrons and holes in the 3D TI QD it is necessary to work at low temperatures of around 1 K.

As an example, here we consider transitions between the states $\kappa = 1$ (at point C) and $\kappa = 2$ (at point B). The matrix elements of the Dirac- α matrix are given by

$$\langle \Phi_f | \alpha | \Phi_I \rangle = \langle \phi_{-}^{\kappa=2} | \sigma | \phi_{+}^{\kappa=1} \rangle + \langle \phi_{+}^{\kappa=2} | \sigma | \phi_{-}^{\kappa=1} \rangle \quad (23)$$

The matrix elements of $\hat{\mathbf{r}}$ are given by

$$\langle \phi_f | \hat{\mathbf{r}} | \phi_I \rangle = \langle \phi_{-}^{\kappa=2} | \hat{\mathbf{r}} | \phi_{-}^{\kappa=1} \rangle + \langle \phi_{+}^{\kappa=2} | \hat{\mathbf{r}} | \phi_{+}^{\kappa=1} \rangle \quad (24)$$

The spherical harmonics can be determined using the Table I. In order to obtain optical selection rules for circular polarizations, it is useful to express the scalar products of the interband and the intraband Hamiltonian in the form $\mathbf{e} \cdot \alpha = \mathbf{e}_z \alpha_z + \mathbf{e}_- \alpha_+ + \mathbf{e}_+ \alpha_-$ and $\mathbf{e} \cdot \hat{\mathbf{r}} = \mathbf{e}_z \hat{r}_z + \mathbf{e}_- \hat{r}_+ + \mathbf{e}_+ \hat{r}_-$, respectively, where $\mathbf{e}_{\pm} = (\mathbf{e}_x \pm i\mathbf{e}_y)/\sqrt{2}$ are the unit vectors of circular polarizations, $\alpha_{\pm} = (\alpha_x \pm i\alpha_y)/\sqrt{2}$, and $\hat{r}_{\pm} = (\hat{x} \pm i\hat{y})/\sqrt{2} = -\sqrt{\frac{4\pi}{3}} r Y_1^{\pm 1}$. Using our spinor states $|\phi_{\mp}\rangle$ and radial wavefunction functions $|f_{\mp}\rangle$ we obtain the following nonzero matrix elements for α :

$$\begin{aligned} \langle \Phi_{\frac{3}{2}, \pm \frac{1}{2}}^{\kappa=2} | \alpha_z | \Phi_{\frac{1}{2}, \pm \frac{1}{2}}^{\kappa=1} \rangle & \stackrel{\pi}{=} \langle \phi_{+, \frac{3}{2}, \pm \frac{1}{2}}^{\kappa=2} | \sigma_z | \phi_{-, \frac{1}{2}, \pm \frac{1}{2}}^{\kappa=1} \rangle \\ & = \frac{2\sqrt{2}}{3} i \langle f_+ | f_- \rangle \end{aligned} \quad (25)$$

$$\begin{aligned} \langle \Phi_{\frac{3}{2}, -\frac{1}{2}}^{\kappa=2} | \alpha_- | \Phi_{\frac{1}{2}, +\frac{1}{2}}^{\kappa=1} \rangle & \stackrel{\sigma^-}{=} \langle \phi_{+, \frac{3}{2}, -\frac{1}{2}}^{\kappa=2} | \sigma_- | \phi_{-, \frac{1}{2}, +\frac{1}{2}}^{\kappa=1} \rangle \\ & = \frac{2}{3} i \langle f_+ | f_- \rangle \end{aligned} \quad (26)$$

$$\begin{aligned} \langle \Phi_{+, \frac{3}{2}, +\frac{1}{2}}^{\kappa=2} | \alpha_+ | \Phi_{-, \frac{1}{2}, -\frac{1}{2}}^{\kappa=1} \rangle & \stackrel{\sigma^+}{=} \langle \phi_{+, \frac{3}{2}, +\frac{1}{2}}^{\kappa=2} | \sigma_+ | \phi_{-, \frac{1}{2}, -\frac{1}{2}}^{\kappa=1} \rangle \\ & = -\frac{2}{3} i \langle f_+ | f_- \rangle \end{aligned} \quad (27)$$

$$\begin{aligned} \langle \Phi_{\frac{3}{2}, +\frac{3}{2}}^{\kappa=2} | \alpha_+ | \Phi_{\frac{1}{2}, +\frac{1}{2}}^{\kappa=1} \rangle & \stackrel{\sigma^+}{=} \langle \phi_{+, \frac{3}{2}, +\frac{3}{2}}^{\kappa=2} | \sigma_+ | \phi_{-, \frac{1}{2}, +\frac{1}{2}}^{\kappa=1} \rangle \\ & = -\frac{2}{\sqrt{3}} i \langle f_+ | f_- \rangle \end{aligned} \quad (28)$$

$$\begin{aligned} \langle \Phi_{+, \frac{3}{2}, -\frac{3}{2}}^{\kappa=2} | \alpha_- | \Phi_{-, \frac{1}{2}, -\frac{1}{2}}^{\kappa=1} \rangle & \stackrel{\sigma^-}{=} \langle \phi_{+, \frac{3}{2}, -\frac{3}{2}}^{\kappa=2} | \sigma_- | \phi_{-, \frac{1}{2}, -\frac{1}{2}}^{\kappa=1} \rangle \\ & = \frac{2}{\sqrt{3}} i \langle f_+ | f_- \rangle \end{aligned} \quad (29)$$

For $\hat{\mathbf{r}}$ we obtain the following nonzero matrix elements:

$$\begin{aligned} \left\langle \Phi_{\frac{3}{2},+\frac{1}{2}}^{\kappa=2} | \hat{z} | \Phi_{\frac{1}{2},+\frac{1}{2}}^{\kappa=1} \right\rangle &= \sqrt{\frac{2}{15}} \langle f_- Y_2^0 | \hat{z} | f_- Y_1^0 \rangle \\ &+ \sqrt{\frac{6}{15}} \langle f_- Y_2^1 | \hat{z} | f_- Y_1^1 \rangle \\ &+ \sqrt{\frac{2}{3}} \langle f_+ Y_1^0 | \hat{z} | f_+ Y_0^0 \rangle, \quad (30) \end{aligned}$$

$$\begin{aligned} \left\langle \Phi_{\frac{3}{2},-\frac{1}{2}}^{\kappa=2} | \hat{z} | \Phi_{\frac{1}{2},-\frac{1}{2}}^{\kappa=1} \right\rangle &= \sqrt{\frac{6}{15}} \langle f_- Y_2^{-1} | \hat{z} | f_- Y_1^{-1} \rangle \\ &+ \sqrt{\frac{2}{15}} \langle f_- Y_2^0 | \hat{z} | f_- Y_1^0 \rangle \\ &+ \sqrt{\frac{2}{3}} \langle f_+ Y_1^0 | \hat{z} | f_+ Y_0^0 \rangle, \quad (31) \end{aligned}$$

$$\begin{aligned} \left\langle \Phi_{\frac{3}{2},-\frac{1}{2}}^{\kappa=2} | \hat{r}_- | \Phi_{\frac{1}{2},+\frac{1}{2}}^{\kappa=1} \right\rangle &= \sqrt{\frac{3}{15}} \langle f_- Y_2^{-1} | \hat{r}_- | f_- Y_1^0 \rangle \\ &+ \sqrt{\frac{4}{15}} \langle f_- Y_2^0 | \hat{r}_- | f_- Y_1^1 \rangle \\ &+ \sqrt{\frac{1}{3}} \langle f_+ Y_1^{-1} | \hat{r}_- | f_+ Y_0^0 \rangle \quad (32) \end{aligned}$$

$$\begin{aligned} \left\langle \Phi_{\frac{3}{2},+\frac{1}{2}}^{\kappa=2} | \hat{r}_+ | \Phi_{\frac{1}{2},-\frac{1}{2}}^{\kappa=1} \right\rangle &= \sqrt{\frac{4}{15}} \langle f_- Y_2^0 | \hat{r}_+ | f_- Y_1^{-1} \rangle \\ &+ \sqrt{\frac{3}{15}} \langle f_- Y_2^1 | \hat{r}_+ | f_- Y_1^0 \rangle \\ &+ \sqrt{\frac{1}{3}} \langle f_+ Y_1^1 | \hat{r}_+ | f_+ Y_0^0 \rangle \quad (33) \end{aligned}$$

$$\begin{aligned} \left\langle \Phi_{\frac{3}{2},+\frac{3}{2}}^{\kappa=2} | \hat{r}_+ | \Phi_{\frac{1}{2},+\frac{1}{2}}^{\kappa=1} \right\rangle &= \sqrt{\frac{1}{15}} \langle f_- Y_2^1 | \hat{r}_+ | f_- Y_1^0 \rangle \\ &+ \sqrt{\frac{8}{15}} \langle f_- Y_2^2 | \hat{r}_+ | f_- Y_1^1 \rangle \\ &+ \langle f_+ Y_1^1 | \hat{r}_+ | f_+ Y_0^0 \rangle, \quad (34) \end{aligned}$$

$$\begin{aligned} \left\langle \Phi_{\frac{3}{2},-\frac{3}{2}}^{\kappa=2} | \hat{r}_- | \Phi_{\frac{1}{2},-\frac{1}{2}}^{\kappa=1} \right\rangle &= \sqrt{\frac{8}{15}} \langle f_- Y_2^{-2} | \hat{r}_- | f_- Y_1^{-1} \rangle \\ &+ \sqrt{\frac{1}{15}} \langle f_- Y_2^{-1} | \hat{r}_- | f_- Y_1^0 \rangle \\ &+ \langle f_+ Y_1^{-1} | \hat{r}_- | f_+ Y_0^0 \rangle, \quad (35) \end{aligned}$$

where $\sigma_+ = (\sigma_x + i\sigma_y)/\sqrt{2} = \begin{pmatrix} 0 & \sqrt{2} \\ 0 & 0 \end{pmatrix}$, $\sigma_- = (\sigma_x - i\sigma_y)/\sqrt{2} = \begin{pmatrix} 0 & 0 \\ \sqrt{2} & 0 \end{pmatrix}$, and the normalization and orthogonality condition $\int_{\Omega} d\Omega Y^{*m',l'}(\Omega) Y^{m,l}(\Omega) = \delta_{l'l'} \delta_{m'm}$ have been used. All other matrix elements are zero.

The transition energy difference between the states $\kappa = 1$ (at point C) and $\kappa = 2$ (at point B) is $0.43\Delta_o$

($\lambda = 7.5\mu\text{m}$) and $1.39\Delta_o$ within the same energy solution and between the negative and positive energy solutions, respectively (see Fig. 4). For $\Delta_o = 93.5$ meV (half of the band gap of PbTe), the corresponding wavelengths are $31\mu\text{m}$ and $9.5\mu\text{m}$. Consider the transitions as shown in Fig. 5. Using the Table I to determine the spherical harmonics, we find that the z -component of the matrix element gives rise to π -transitions with $\kappa = 2, m_j = 1/2 \longleftrightarrow \kappa = 2, m_j = 1/2$ and with $\kappa = 2, m_j = -1/2 \longleftrightarrow \kappa = 1, m_j = -1/2$. Thus, these π -transitions are coupled to light polarized linearly in z -direction. The $x - iy$ - and $x + iy$ -components of the matrix element give rise to the σ^+ -transition with $\kappa = 2, m_j = +1/2 \longleftrightarrow \kappa = 1, m_j = -1/2$ and with $\kappa = 2, m_j = 3/2 \longleftrightarrow \kappa = 1, m_j = 1/2$ and to the σ^- -transition with $\kappa = 2, m_j = -1/2 \longleftrightarrow \kappa = 1, m_j = +1/2$ and with $\kappa = 2, m_j = -3/2 \longleftrightarrow \kappa = 1, m_j = -1/2$. Thus, σ^+ -transition and σ^- -transition are coupled to the right and left circularly polarized light, respectively. We can take advantage of these strict optical selection rules to implement the semi-classical and quantum Faraday effect shown below. The overlap integrals $\langle f_+ (\kappa = 2) | f_- (\kappa = 1) \rangle$ and $\langle f_- (\kappa = 2) | f_+ (\kappa = 1) \rangle$ for the transitions between the points B and C (in Fig. 2) are evaluated to be 0.31 and 0.24, respectively. The Kane energy, $E_p = 2P_{\perp}^2/m_o$, is calculated to be 7.3 eV which is about 3 times smaller than the Kane energy value of 22.7 eV for GaAs.^{53,54} The smaller Kane energy here is due to the fact that the Fermi velocity is an order of magnitude smaller than the Fermi velocity in GaAs. The polarization matrix elements of \hat{r}_{\pm} accounts for the strength of the in-plane intraband transitions at the band crossing. We calculate the magnitude of the matrix elements for σ^{\mp} transitions and find that $e \left| \left\langle \Phi_{\frac{3}{2},-\frac{1}{2}}^{\kappa=2} | \hat{r}_- | \Phi_{\frac{1}{2},+\frac{1}{2}}^{\kappa=1} \right\rangle \right| = e \left| \left\langle \Phi_{\frac{3}{2},+\frac{1}{2}}^{\kappa=2} | \hat{r}_+ | \Phi_{\frac{1}{2},-\frac{1}{2}}^{\kappa=1} \right\rangle \right| = 128$ Debye and $e \left| \left\langle \Phi_{\frac{3}{2},+\frac{3}{2}}^{\kappa=2} | \hat{r}_+ | \Phi_{\frac{1}{2},+\frac{1}{2}}^{\kappa=1} \right\rangle \right| = e \left| \left\langle \Phi_{\frac{3}{2},-\frac{3}{2}}^{\kappa=2} | \hat{r}_- | \Phi_{\frac{1}{2},-\frac{1}{2}}^{\kappa=1} \right\rangle \right| = 221$ Debye. For the π transitions we find the magnitude of the matrix elements as, $e \left| \left\langle \Phi_{\frac{3}{2},+\frac{1}{2}}^{\kappa=2} | \hat{z} | \Phi_{\frac{1}{2},+\frac{1}{2}}^{\kappa=1} \right\rangle \right| = e \left| \left\langle \Phi_{\frac{3}{2},-\frac{1}{2}}^{\kappa=2} | \hat{z} | \Phi_{\frac{1}{2},-\frac{1}{2}}^{\kappa=1} \right\rangle \right| = 181$ Debye.

V. FARADAY EFFECT FOR 3D TI QDS

In Refs. 43,44,55–57 we showed that the single-photon Faraday rotation cannot only be used for quantum spin memory but also for quantum teleportation and quantum computing with wide-bandgap semiconductor QDs. In Ref. 58 we showed that the conditional Faraday rotation can be used for optical switching of classical information. In Ref. 59 we proposed a single-photon Mach-Zehnder interferometer for quantum networks based on the single-photon Faraday effect. In Ref. 60 a single spin in a wide-bandgap semiconductor QD was detected using the Faraday rotation. In order to implement these appli-

cations with 3D TI QDs, we need strict optical selection rules for the circular polarization of the photons. Since, indeed, for 3D TI QDs we obtain strict optical selection rules for circular polarization of photons, we suggest that it is possible to implement quantum memory, quantum teleportation, and quantum computing using the single-photon Faraday rotation in 3D TI QDs. In order to prove this conjecture, we derive the Faraday effect for 3D TI QDs. For the derivation of the Faraday effect for a classical laser beam due to Pauli exclusion principle we are going to follow Ref. 61. Below in Sec. VII we are going to derive also the Faraday effect for a single photon using quantum optical calculations, where we use Ref. 62.

In order to simplify the notation, we write the light-matter interaction Hamiltonian as $H_{int} = ev\mathbf{\alpha} \cdot \mathbf{A} - e\hat{\mathbf{r}} \cdot \mathbf{E}$. Without loss of generality, the anisotropy coming from the band velocity can be introduced back into the solutions at a later time. Since the incident light is a plane wave with wavevector \mathbf{q} and frequency ω and the electric field component is $E = -\partial\mathbf{A}/\partial t$, the interaction Hamiltonian reads

$$H_{int} = \frac{ePE_0}{im_0\omega} \left(e^{i(\mathbf{q}\cdot\mathbf{r}-\omega t)} - e^{-i(\mathbf{q}\cdot\mathbf{r}-\omega t)} \right) \mathbf{e} \cdot \mathbf{\alpha} - eE_0 \left(e^{i(\mathbf{q}\cdot\mathbf{r}-\omega t)} + e^{-i(\mathbf{q}\cdot\mathbf{r}-\omega t)} \right) \mathbf{e} \cdot \hat{\mathbf{r}} \quad (36)$$

where $P = m_0v$ is the Kane interband matrix element. The transition rate for a single 3D TI QD can then be calculated using Fermi's golden rule,

$$W_{fI} = \frac{2\pi}{\hbar} (eE_0)^2 \left| \langle \Phi_f | \frac{P}{im_0\omega} \mathbf{e} \cdot \mathbf{\alpha} + \mathbf{e} \cdot \hat{\mathbf{r}} | \Phi_I \rangle \right|^2 \times f(\varepsilon_I) [1 - f(\varepsilon_f)] \delta(\varepsilon_f - \varepsilon_I \mp \hbar\omega) \quad (37)$$

where $f(\varepsilon) = \left[\exp\left(\frac{\varepsilon - \varepsilon_F}{k_B T}\right) + 1 \right]^{-1}$ is the Fermi-Dirac distribution function, ε_F is the Fermi energy, $|\Phi_I\rangle$ denotes the initial Weyl state, $|\Phi_f\rangle$ denotes the final Weyl state, and the - sign in front of $\hbar\omega$ corresponds to absorption and the + sign to emission. Thus, the absorption of energy per spin state is $\mathcal{P} = \hbar\omega \sum_{I,f} W_{fI}$. Comparing with the total power $\mathcal{P} = 2\sigma_1 V E_0^2$ dissipated in the system volume V , where $\sigma = \sigma_1 + i\sigma_2$ is the complex conductivity, and including absorption and emission, it follows that the real part of the conductivity is

$$\sigma_1 = \frac{\pi e^2 \omega}{V} \sum_{I,f} \left| \langle \Phi_f | \frac{P}{im_0\omega} \mathbf{e} \cdot \mathbf{\alpha} + \mathbf{e} \cdot \hat{\mathbf{r}} | \Phi_I \rangle \right|^2 \times [f(\varepsilon_I) - f(\varepsilon_f)] \delta(\varepsilon_f - \varepsilon_I - \hbar\omega) \quad (38)$$

which can be written in terms of the oscillator strengths

$$f_{fI} = (2m_0\omega_{fI}/\hbar) \left| \langle \Phi_f | \frac{P}{im_0\omega} \mathbf{e} \cdot \mathbf{\alpha} + \mathbf{e} \cdot \hat{\mathbf{r}} | \Phi_I \rangle \right|^2, \quad \sigma_1(\omega) = \frac{\pi e^2}{2m_0V} \sum_{fI} f_{fI} [f(\varepsilon_I) - f(\varepsilon_f)] \delta(\varepsilon_f - \varepsilon_I - \hbar\omega) \quad (39)$$

Using the relation $\epsilon_r = 1 + \frac{i}{\omega\epsilon_0}\sigma$, where ϵ_0 is the free-space permittivity, between the complex conductivity and the complex dielectric function $\epsilon_r = \epsilon_1 + i\epsilon_2$ and taking advantage of the Kramers-Kronig relations the complex dielectric function is given by

$$\epsilon_r(\omega) = 1 - \frac{e^2}{\epsilon_0 m_0 V} \sum_{fI} \frac{f_{fI} [f(\varepsilon_I) - f(\varepsilon_f)]}{(\omega^2 - \omega_{fI}^2) + i\gamma\omega} \quad (40)$$

In order to describe the Faraday rotation, we need to consider only the states $|\Phi_{\frac{1}{2}, \pm \frac{1}{2}}^{\kappa=1}\rangle$, $|\Phi_{\frac{3}{2}, \pm \frac{1}{2}}^{\kappa=2}\rangle$, and $|\Phi_{\frac{3}{2}, \pm \frac{3}{2}}^{\kappa=2}\rangle$ coupled by circular polarized light (see Fig. 5). We denote their energy difference by $\hbar\omega_0 = \varepsilon_{\kappa=2} - \varepsilon_{\kappa=1}$. Defining the the quantity

$$M_{f;I} = \left| \langle \Phi_f^{\kappa=2} | \frac{P}{im_0\omega} \mathbf{e} \cdot \mathbf{\alpha} + \mathbf{e} \cdot \hat{\mathbf{r}} | \Phi_I^{\kappa=1} \rangle \right|^2 \times [f(\varepsilon_I) - f(\varepsilon_f)] \quad (41)$$

we can rewrite the complex dielectric function as

$$\epsilon_r(\omega) = \epsilon_{QD}(\omega) - \frac{2e^2\rho\omega}{\epsilon_0\hbar} \left\{ \frac{M_{\frac{3}{2}, +\frac{3}{2}; \frac{1}{2}, +\frac{1}{2}} + M_{\frac{3}{2}, -\frac{3}{2}; \frac{1}{2}, -\frac{1}{2}}}{(\omega^2 - \omega_0^2) + i\gamma\omega} + \frac{M_{\frac{3}{2}, +\frac{1}{2}; \frac{1}{2}, -\frac{1}{2}} + M_{\frac{3}{2}, -\frac{1}{2}; \frac{1}{2}, +\frac{1}{2}}}{[\omega^2 - (\omega_0 + \Delta_S/\hbar)^2] + i\gamma\omega} \right\} \quad (42)$$

where Δ_S is the Stark energy shift (see below). Summation over the other states is included in $\epsilon_{QD}(\omega)$, which is the dielectric function of $\text{Pb}_{0.63}\text{Sn}_{0.37}\text{Te}$, corresponding to the material at the interface. $\rho = 1/V$ is the 3D TI QD density. This expression can be split into a component of the dielectric function for the right circular polarization,

$$\epsilon_+(\omega) = \epsilon_{QD}(\omega) - \frac{2e^2\rho\omega}{\epsilon_0\hbar} \left\{ \frac{M_{\frac{3}{2}, +\frac{3}{2}; \frac{1}{2}, +\frac{1}{2}}}{(\omega^2 - \omega_0^2) + i\gamma\omega} + \frac{M_{\frac{3}{2}, +\frac{1}{2}; \frac{1}{2}, -\frac{1}{2}}}{[\omega^2 - (\omega_0 + \Delta_S/\hbar)^2] + i\gamma\omega} \right\} \quad (43)$$

and a component of the dielectric function for the left circular polarization,

$$\epsilon_-(\omega) = \epsilon_{QD}(\omega) - \frac{2e^2\rho\omega}{\epsilon_0\hbar} \left\{ \frac{M_{\frac{3}{2}, -\frac{3}{2}; \frac{1}{2}, -\frac{1}{2}}}{(\omega^2 - \omega_0^2) + i\gamma\omega} + \frac{M_{\frac{3}{2}, -\frac{1}{2}; \frac{1}{2}, +\frac{1}{2}}}{[\omega^2 - (\omega_0 + \Delta_S/\hbar)^2] + i\gamma\omega} \right\} \quad (44)$$

Consequently, the indices of refraction for right and left circular polarization are given by $n_{\pm} = \sqrt{\epsilon_{\pm}}$. Assuming that the length of the material is L , the Faraday rotation can now be understood by considering the electric component of the plane wave after passing through the material at position $z = L$,

$$\begin{aligned} \mathbf{E}(z=L) &= \frac{E_0}{\sqrt{2}} (e^{ik-L}\mathbf{e}_+ + e^{ik+L}\mathbf{e}_-) e^{-i\omega t} \\ &= E_0 \left(\cos \frac{\Delta n \omega L}{c} \mathbf{e}_x + \sin \frac{\Delta n \omega L}{c} \mathbf{e}_y \right) \\ &\quad \times e^{i(kL - \omega t + (n-1)\frac{\omega L}{c})} \end{aligned} \quad (45)$$

where $\mathbf{e}_\pm = (\mathbf{e}_x \pm i\mathbf{e}_y)/\sqrt{2}$ are the circular polarization unit vectors, $n = (n_+ + n_-)/2$ is the average index of refraction, c is the speed of light in vacuum, and $\Delta n = n_+ - n_-$ is the difference in index of refraction between right and left circular polarization. Thus, the Faraday rotation angle is given by

$$\vartheta = \frac{\Delta n \omega L}{2c}. \quad (46)$$

This formula shows that the Faraday rotation angle depends on the populations of the states $|\Phi_{\frac{1}{2}, \pm \frac{1}{2}}^{\kappa=1}\rangle$, $|\Phi_{\frac{3}{2}, \pm \frac{1}{2}}^{\kappa=2}\rangle$, and $|\Phi_{\frac{3}{2}, \pm \frac{3}{2}}^{\kappa=2}\rangle$, as determined by the Fermi functions, which can be used in the quasi-equilibrium, i.e. when the time is much smaller than the electron-hole recombination time. A similar Faraday effect has already been successfully used to experimentally detect a single spin inside a GaAs QD.⁶⁰

VI. QUANTUM MEMORY WITH 3D TI QDS

Let us first describe the quantum memory with 3D TI QDs. In order to obtain the maximum Faraday effect, it is possible to apply an oscillating electric field $\mathbf{E}(t)$ pointing in z -direction, which splits the $|\Phi_{\frac{3}{2}, \pm \frac{1}{2}}^{\kappa=2}\rangle$ states from the $|\Phi_{\frac{3}{2}, \pm \frac{3}{2}}^{\kappa=2}\rangle$ states due to the optical Stark effect (see Fig. 6). The coupling to the electric field is described by the relativistic Stark Hamiltonian

$$H_S = \begin{pmatrix} -ezE_z e^{i\omega_S t} & ev_{\parallel} \sigma_z A_z \\ ev_{\parallel} \sigma_z A_z & -ezE_z e^{i\omega_S t} \end{pmatrix}, \quad (47)$$

where $E_z(t) = E_S(e^{i\omega_S t} + e^{-i\omega_S t})$ and thus $A_z(t) = \frac{iE_S}{\omega_S}(e^{i\omega_S t} - e^{-i\omega_S t})$. In second-order perturbation theory we obtain the quadratic Stark effect. The only nonzero contributions come from the matrix element coupling the $|\Phi_{\frac{3}{2}, \pm \frac{1}{2}}^{\kappa=2}\rangle$ state to the $|\Phi_{\frac{1}{2}, \pm \frac{1}{2}}^{\kappa=1}\rangle$ state, and from the matrix element coupling the $|\Phi_{\frac{3}{2}, -\frac{1}{2}}^{\kappa=2}\rangle$ state to the $|\Phi_{\frac{1}{2}, -\frac{1}{2}}^{\kappa=1}\rangle$ state. This yields the Stark energy shift

$$\begin{aligned} \Delta_S &= e^2 E_S^2 \frac{\left| \left\langle \Phi_{\frac{1}{2}, \pm \frac{1}{2}}^{\kappa=1} \left| \frac{P}{im_0 \omega_S} \alpha_z + z \right| \Phi_{\frac{3}{2}, \pm \frac{1}{2}}^{\kappa=2} \right\rangle \right|^2}{\hbar(\omega_0 - \omega_S)} \\ &= e^2 E_S^2 \frac{\left| \left\langle \Phi_{\frac{1}{2}, -\frac{1}{2}}^{\kappa=1} \left| \frac{P}{im_0 \omega_S} \alpha_z + z \right| \Phi_{\frac{3}{2}, -\frac{1}{2}}^{\kappa=2} \right\rangle \right|^2}{\hbar(\omega_0 - \omega_S)} \end{aligned} \quad (48)$$

The Stark energy shift can be determined by applying an oscillating electric field whose amplitude is measured along z -direction. The amplitude of the electric field can be calculated as $|E_S| = \sqrt{2S n / A \epsilon_0 c}$, where S is the power of the laser, n is the index of refraction of the medium through which the light propagates and A is the area of the aperture of the laser source. A laser

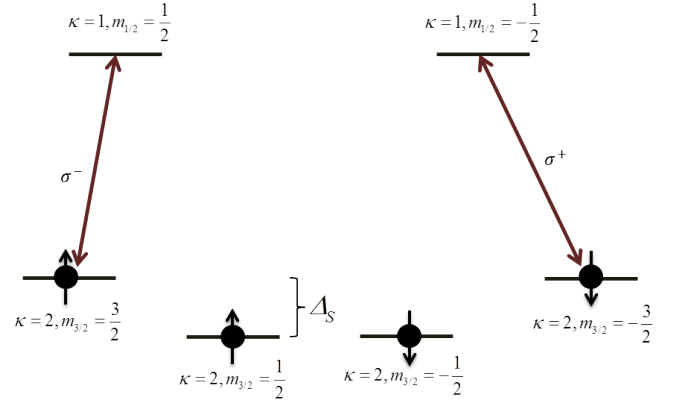


Figure 6: This is one possible level configuration that can be used for the implementation of the quantum memory.

power of 1 mW with energy $\hbar\omega_S = 30$ meV and area of the aperture of $1 \mu\text{m}^2$ in a medium with $n = 5.7$ (for $\text{Pb}_{0.68}\text{Sn}_{0.32}\text{Te}$ at room temperature) can produce an electric field of 1.46×10^7 V/m. Using the Fermi velocity of $v_{\parallel} = 2.24 \times 10^5$ m/s to calculate P , our calculations show that the matrix element in Eq. (48) is $e \left| \left\langle \Phi_{\frac{1}{2}, \pm \frac{1}{2}}^{\kappa=1} \left| \frac{P}{im_0 \omega_S} \alpha_z + z \right| \Phi_{\frac{3}{2}, \pm \frac{1}{2}}^{\kappa=2} \right\rangle \right| = 410$ Debye. With the transition energy difference of $\hbar\omega_0 = 130$ meV we get a Stark energy shift of $\Delta_S = 14$ meV.

It has already been shown experimentally that single-electron loading is possible in 3D TI QDs.²⁴ We focus on two possible level configurations due to the electron-hole symmetry in 3D TI QDs:

1. Fig. 6 shows the first level configuration where the electron states are given by the s-like states $|\Phi_{\frac{1}{2}, \pm \frac{1}{2}}^{\kappa=1}\rangle$ and the hole states are given by the p-like states $|\Phi_{\frac{3}{2}, \pm \frac{1}{2}}^{\kappa=2}\rangle$ and $|\Phi_{\frac{3}{2}, \pm \frac{3}{2}}^{\kappa=2}\rangle$.
2. Fig. 7 shows the second level configuration where the electron states are given by the p-like states $|\Phi_{\frac{3}{2}, \pm \frac{1}{2}}^{\kappa=2}\rangle$ and $|\Phi_{\frac{3}{2}, \pm \frac{3}{2}}^{\kappa=2}\rangle$ and the hole states are given by the s-like states $|\Phi_{\frac{1}{2}, \pm \frac{1}{2}}^{\kappa=1}\rangle$.

Only due to the symmetry between positive- and negative-energy solutions in a 3D TI QD it is possible to choose either of these two level configurations.

Then, using the optical selection rules shown in Fig. 5, we can use right circularly polarized light to create an e-h pair with polarization +1, as shown in Fig. 6. This corresponds to writing the information +1 on the 3D TI QD. Alternatively, we can use left circularly polarized light to create an e-h pair with polarization -1, as shown in Fig. 6. This corresponds to writing the information -1 on the 3D TI QD.

If we want to read out the information several times before the electron-hole recombination, we can take advantage of the Faraday effect due to the Pauli exclusion principle. For this method, we apply a π -pulse of right

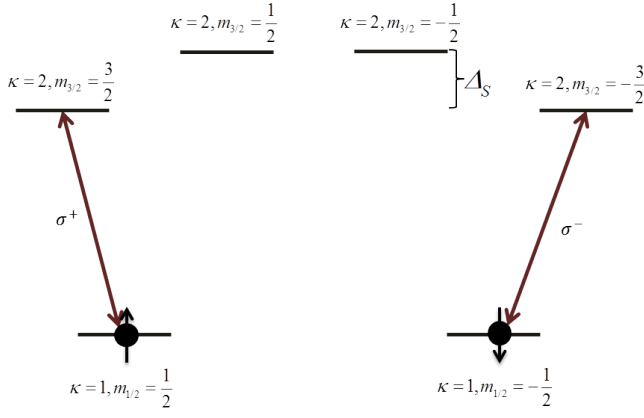


Figure 7: This is another possible level configuration that can be used for the implementation of the quantum memory.

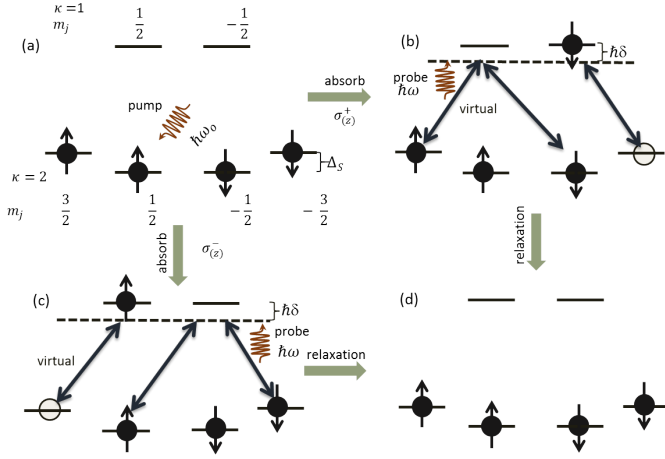


Figure 8: (a) The incident photon can be either right or left circularly polarized. The initial level configuration is the one shown in Fig. 6. (b) If the photon is right circularly polarized, an e-h pair with +1 polarization is created, which can be probed using off-resonant linearly polarized light that acquires a negative Faraday rotation angle through virtual excitation of an e-h pair and virtual recombinations of the present e-h pair. (c) If the photon is left circularly polarized, an e-h pair with -1 polarization is created, which can be probed using off-resonant linearly polarized light that acquires a positive Faraday rotation angle through virtual excitation of an e-h pair and virtual recombinations of the present e-h pair. (d) After the probing, the e-h pair relaxes into the ground state configuration.

or left circularly polarized light, thereby writing the information +1 or -1, respectively, as shown in Fig. 8. For +1 polarization, the Fermi functions, corresponding to populations in quasi-equilibrium, are $f(\varepsilon_{\frac{1}{2},+\frac{1}{2}}) = 0$, $f(\varepsilon_{\frac{1}{2},-\frac{1}{2}}) = 1$, $f(\varepsilon_{\frac{3}{2},+\frac{3}{2}}) = 1$, $f(\varepsilon_{\frac{3}{2},+\frac{1}{2}}) = 1$, $f(\varepsilon_{\frac{3}{2},-\frac{1}{2}}) = 1$ and $f(\varepsilon_{\frac{3}{2},-\frac{3}{2}}) = 0$. For -1 polarization, the Fermi functions, corresponding to populations

in quasi-equilibrium, are $f(\varepsilon_{\frac{1}{2},+\frac{1}{2}}) = 1$, $f(\varepsilon_{\frac{1}{2},-\frac{1}{2}}) = 0$, $f(\varepsilon_{\frac{3}{2},+\frac{3}{2}}) = 0$, $f(\varepsilon_{\frac{3}{2},+\frac{1}{2}}) = 1$, $f(\varepsilon_{\frac{3}{2},-\frac{1}{2}}) = 1$ and $f(\varepsilon_{\frac{3}{2},-\frac{3}{2}}) = 1$. Since the off-resonant interaction does not destroy the quantum state on the 3D TI QD, the information can be read out several times before recombination. These results are in complete agreement with the quantum-optical calculations shown below.

Let us assume a right circularly polarized pump pulse of energy $\hbar\omega_0$ excites an e-h pair with polarization +1 due to the σ^+ -transition from the state $|\Phi_{\frac{3}{2},-\frac{3}{2}}^{\kappa=2}\rangle$ to the state $|\Phi_{\frac{1}{2},-\frac{1}{2}}^{\kappa=1}\rangle$ in the level configuration shown in Fig. 6. Then a linearly polarized probe pulse of energy $\hbar\omega$ with certain detuning energy is applied to read it out. There are three virtual transitions that can occur while probing, one σ^- transition: $|\Phi_{\frac{3}{2},\frac{3}{2}}^{\kappa=2}\rangle \leftrightarrow |\Phi_{\frac{1}{2},+\frac{1}{2}}^{\kappa=1}\rangle$ and two σ^+ transitions: $|\Phi_{\frac{3}{2},-\frac{3}{2}}^{\kappa=1}\rangle \leftrightarrow |\Phi_{\frac{3}{2},-\frac{3}{2}}^{\kappa=2}\rangle$ and $|\Phi_{\frac{3}{2},-\frac{1}{2}}^{\kappa=2}\rangle \leftrightarrow |\Phi_{\frac{1}{2},+\frac{1}{2}}^{\kappa=1}\rangle$. The matrix elements in the Eq. 46 are calculated using the Fermi functions in the quasi-equilibrium. The matrix elements are evaluated to be $M_{\frac{3}{2},\pm\frac{3}{2};\frac{1}{2},\pm\frac{1}{2}} = \mp 8.07 \times 10^{-18} \text{ m}^2$ and $M_{\frac{3}{2},-\frac{1}{2};\frac{1}{2},+\frac{1}{2}} = -2.67 \times 10^{-18} \text{ m}^2$. The sign of the matrix elements $M_{f,I}$ is determined by the Fermi functions. The corresponding dipole moments are 454 Debye and 261 Debye, respectively. For a quantitative estimate, we choose a transition energy gap between the negative and positive energy solution of $\hbar\omega_o = 130 \text{ meV}$, a linearly polarized probe pulse with detuning energy of $\hbar\delta = 1 \text{ meV}$ and a cavity photon with a bandwidth of $\hbar\gamma = 100 \mu\text{eV}$.^{60,63} We further assume that there is a single QD in a slab material of length $L = 0.1 \mu\text{m}$. With these values for our 3D TI QD of size 3.5 nm we obtain the real part of the Faraday rotation angle of $\vartheta_{+1} = -624 \mu\text{rad}$. This Faraday rotation angle is well above the angle value that has been measured for the experimental detection of a single spin in GaAs QDs.⁶⁰ A similar calculation can be done for a left circularly polarized pump pulse that excites an e-h pair with polarization -1 due to a σ^- -transition from the state $|\Phi_{\frac{3}{2},+\frac{3}{2}}^{\kappa=2}\rangle$ to the state $|\Phi_{\frac{1}{2},+\frac{1}{2}}^{\kappa=1}\rangle$. Due to the symmetry of the positive- and negative-energy solutions in 3D TI QDs, a large variety of level configurations can be considered to achieve the Faraday effect.

The largest dipole moment of 452 Debye is one order of magnitude larger than the typical value of 75 Debye for GaAs QDs,⁶⁵ and two orders of magnitude larger than the typical value of a few Debye for atoms.⁶⁶ This large strength of the coupling of infrared light to 3D TI QDs can partially compensate the weak overlap of the photon with the 3D TI QD, which is due to the wavelength of the infrared light being so much larger than the size of the 3D TI QD.

VII. SINGLE-PHOTON FARADAY EFFECT FOR 3D TI QDS

Let us consider a 3D TI QD in the level configuration shown in Fig. 6 inside a cavity. We define $c_{1\pm}$, $c_{2\pm}$ and $c_{3\pm}$ as the annihilation operators of the states $|\Phi_{\frac{3}{2},\pm\frac{1}{2}}^{\kappa=2}\rangle$, $|\Phi_{\frac{3}{2},\pm\frac{3}{2}}^{\kappa=2}\rangle$, and $|\Phi_{\frac{1}{2},\pm\frac{1}{2}}^{\kappa=1}\rangle$, respectively. Then the Jaynes-Cummings model⁶² gives rise to the Hamiltonian $H = H_p + H_{QD} + H_{p-QD}$, where

$$H_p = \hbar\omega_c (a_+^\dagger a_+ + a_-^\dagger a_-), \quad (49)$$

$$H_{QD} = \sum_{j=1}^3 \hbar\omega_j (c_{j+}^\dagger c_{j+} + c_{j-}^\dagger c_{j-}),$$

$$H_{p-QD} = \hbar g_1 (a_+ c_{3+}^\dagger c_{1-} + a_- c_{3-}^\dagger c_{1+}) + h.c. \quad (50)$$

$$+ \hbar g_2 (a_+ c_{3-}^\dagger c_{2-} + a_- c_{3+}^\dagger c_{2+}) + h.c. \quad (51)$$

are the cavity photon Hamiltonian, the QD Hamiltonian describing the Weyl states, and the interaction Hamiltonian describing the photon-QD interaction, respectively. We can safely neglect the vacuum energy $\hbar\omega_c/2$ per mode. The photon-QD coupling constants are given by $\hbar g_1 = \sqrt{\hbar\omega/2\epsilon_0 V_0} e \langle \Phi_{\frac{3}{2},\pm\frac{1}{2}}^{\kappa=2} | \frac{P}{im_0\omega} \mathbf{e} \cdot \boldsymbol{\alpha} + \mathbf{e} \cdot \hat{\mathbf{r}} | \Phi_{\frac{1}{2},\mp\frac{1}{2}}^{\kappa=1} \rangle$ and $\hbar g_2 = \sqrt{\hbar\omega/2\epsilon_0 V_0} e \langle \Phi_{\frac{3}{2},\pm\frac{3}{2}}^{\kappa=2} | \frac{P}{im_0\omega} \mathbf{e} \cdot \boldsymbol{\alpha} + \mathbf{e} \cdot \hat{\mathbf{r}} | \Phi_{\frac{1}{2},\pm\frac{1}{2}}^{\kappa=1} \rangle$, where V_0 is the modal volume. After switching to the electron-hole picture using the new electron and hole operators $c_{\pm} = c_{3\pm}$ and $v_{j\mp}^\dagger = c_{j\pm}^\dagger$ for $j = 1, 2$, we obtain

$$H_p = \hbar\omega_c (a_+^\dagger a_+ + a_-^\dagger a_-),$$

$$H_{QD} = \hbar\omega_3 (c_{+}^\dagger c_{+} + c_{-}^\dagger c_{-}) + \sum_{j=1}^2 \hbar\omega_j (v_{j+}^\dagger v_{j+} + v_{j-}^\dagger v_{j-}), \quad (52)$$

$$H_{int} = \hbar g_1 (a_+ c_{+}^\dagger v_{1+}^\dagger + a_- c_{-}^\dagger v_{1-}^\dagger) + h.c. \\ + \hbar g_2 (a_+ c_{-}^\dagger v_{2+}^\dagger + a_- c_{+}^\dagger v_{2-}^\dagger) + h.c. \quad (53)$$

where $\hbar\omega_3 - \hbar\omega_2 = \hbar\omega_c + \hbar\delta$ and $\hbar\omega_2 - \hbar\omega_1 = \Delta_S$. Since the interaction between the EM fields and the QDs is off-resonant, we can apply an adiabatic approximation. For that, let us calculate the time evolution of the polarization operators $p_{j\sigma\sigma'}(t) = v_{j\sigma} c_{\sigma'}$ (coherences) by means of the Heisenberg equation of motion, i.e.

$$\frac{\partial p_{j\sigma\sigma'}(t)}{\partial t} = \frac{1}{i\hbar} [p_{j\sigma\sigma'}(t), H] = \frac{1}{i\hbar} [p_{j\sigma\sigma'}(t), H_{QD} + H_{int}] \quad (56)$$

Since

$$[p_{j\sigma\sigma'}, p_{\lambda j'\lambda'}^\dagger] = v_{j\sigma} v_{j'\lambda'}^\dagger \delta_{\sigma'\lambda} - c_{\lambda}^\dagger c_{\sigma'} \delta_{jj'} \delta_{\sigma\lambda'} \\ = (1 - v_{j'\lambda'}^\dagger v_{j\sigma}) \delta_{\sigma'\lambda} - c_{\lambda}^\dagger c_{\sigma'} \delta_{jj'} \delta_{\sigma\lambda'} \quad (57)$$

and

$$[p_{j\sigma\sigma'}, c_{\lambda}^\dagger c_{\lambda}] = p_{j\sigma\lambda} \delta_{\sigma'\lambda} \\ [p_{j\sigma\sigma'}, v_{j'\lambda}^\dagger v_{j'\lambda}] = p_{j'\lambda\sigma'} \delta_{jj'} \delta_{\sigma\lambda} \quad (58)$$

we obtain

$$i \frac{\partial p_{1\pm\pm}}{\partial t} = \left(\omega_c + \delta + \frac{\Delta_S}{\hbar} \right) p_{1\pm\pm} \\ + g_1 a_{\pm} (1 - c_{\pm}^\dagger c_{\pm} - v_{1\pm}^\dagger v_{1\pm}) \\ + g_2 a_{\mp} (1 - v_{2\mp}^\dagger v_{2\mp}), \quad (59)$$

$$i \frac{\partial p_{2\pm\mp}}{\partial t} = (\omega_c + \delta) p_{2\pm\mp} \\ + g_1 a_{\mp} (1 - v_{1\mp}^\dagger v_{2\pm}) \\ + g_2 a_{\pm} (1 - c_{\mp}^\dagger c_{\mp} - v_{2\pm}^\dagger v_{2\pm}), \quad (60)$$

where the + (-) sign denotes the polarization with right (left) circular polarization. Since the states $|\Phi_{\frac{3}{2},\pm\frac{1}{2}}^{\kappa=2}\rangle$ and $|\Phi_{\frac{3}{2},\pm\frac{3}{2}}^{\kappa=2}\rangle$ are not resonantly coupled, no coherences $v_{2\pm} v_{1\mp}^\dagger$ and $v_{2\pm} v_{1\mp}^\dagger$ are created. Therefore they are zero. It is possible to transform to the rotating frame by means of $\tilde{p}_{1\pm\pm} = p_{1\pm\pm} e^{-i\omega_c t}$, $\tilde{p}_{2\pm\mp} = p_{2\pm\mp} e^{-i\omega_c t}$ and $\tilde{a}_{\pm} = a_{\pm} e^{-i\omega_c t}$, resulting in

$$i \frac{\partial p_{1\pm\pm}}{\partial t} = \left(\delta + \frac{\Delta_S}{\hbar} \right) p_{1\pm\pm} \\ + g_1 a_{\pm} (1 - c_{\pm}^\dagger c_{\pm} - v_{1\pm}^\dagger v_{1\pm}), \quad (61)$$

$$(52) \quad i \frac{\partial p_{2\pm\mp}}{\partial t} = \delta p_{2\pm\mp} + g_2 a_{\pm} (1 - c_{\mp}^\dagger c_{\mp} - v_{2\pm}^\dagger v_{2\pm}) \quad (62)$$

where we omitted the tildes. The Heisenberg equations for the polarization operators $p_{1\pm\pm}$ and $p_{2\pm\mp}$ can be obtained by taking the Hermitian conjugate. Since in the case of the Faraday effect the photon is off-resonant with the energy difference $\hbar\omega_{21} = \hbar\omega_2 - \hbar\omega_1$, we can apply the adiabatic approximation, which corresponds to setting the time derivatives in the Heisenberg equations to zero, i.e. taking the stationary limit. Then we obtain

$$p_{1\pm\pm} = - \frac{g_1 a_{\pm} (1 - c_{\pm}^\dagger c_{\pm} - v_{1\pm}^\dagger v_{1\pm})}{(\delta + \frac{\Delta_S}{\hbar})}, \quad (63)$$

$$p_{2\pm\mp} = - \frac{g_2 a_{\pm} (1 - c_{\mp}^\dagger c_{\mp} - v_{2\pm}^\dagger v_{2\pm})}{\delta}. \quad (64)$$

Inserting this result into the interaction Hamiltonian leads to an effective interaction Hamiltonian of the form

$$H_{int}^{eff} = - \frac{\hbar g_1^2}{(\delta + \frac{\Delta_S}{\hbar})} \sum_{\sigma} (2a_{\sigma}^\dagger a_{\sigma} + 1) (1 - c_{\sigma}^\dagger c_{\sigma} - v_{1\sigma}^\dagger v_{1\sigma}) \\ - \frac{\hbar g_2^2}{\delta} \sum_{\sigma} (2a_{\sigma}^\dagger a_{\sigma} + 1) (1 - c_{\sigma}^\dagger c_{\sigma} - v_{1\sigma}^\dagger v_{1\sigma}), \quad (65)$$

where $\bar{\sigma}$ has the opposite sign of σ . It becomes obvious that if electrons or holes are present, the effective interaction can be suppressed. Most importantly, this suppression of interaction depends on the spin of the present electrons or holes. This is exactly the mechanism for the Faraday effect due to Pauli exclusion principle. Let us now calculate the time evolution of the photon operator in the rotating frame under the effective interaction Hamiltonian, i.e.

$$\begin{aligned} i\hbar \frac{\partial a_{\pm}}{\partial t} &= [a_{\pm}, H_{int}^{eff}] \\ &= -2a_{\pm} \left[\left(\frac{\hbar g_1^2}{\delta + \frac{\Delta_S}{\hbar}} \right) (1 - c_{\pm}^{\dagger} c_{\pm} - v_{1\pm}^{\dagger} v_{1\pm}) \right. \\ &\quad \left. + \left(\frac{\hbar g_2^2}{\delta} \right) (1 - c_{\mp}^{\dagger} c_{\mp} - v_{2\pm}^{\dagger} v_{2\pm}) \right], \end{aligned} \quad (66)$$

resulting in the solution

$$\begin{aligned} a_{\pm}(t) &= a_{\pm}(0) \exp \left\{ -i \left[\frac{2g_1^2}{\delta + \frac{\Delta_S}{\hbar}} (1 - c_{\pm}^{\dagger} c_{\pm} - v_{1\pm}^{\dagger} v_{1\pm}) \right. \right. \\ &\quad \left. \left. + \frac{2g_2^2}{\delta} (1 - c_{\mp}^{\dagger} c_{\mp} - v_{2\pm}^{\dagger} v_{2\pm}) \right] t \right\}. \end{aligned} \quad (67)$$

This formula is the main result of this section. It shows that the Faraday rotation of the linearly polarized light depends strongly on the presence of electrons and holes due to the Pauli exclusion principle.

VIII. QUANTUM TELEPORTATION AND QUANTUM COMPUTING WITH 3D TI QDS

Here we show that the single-photon Faraday rotation can be used to entangle a single photon with either a single e-h pair, a single electron, or a single hole. This entanglement can be used as a resource to implement optically mediated quantum teleportation and quantum computing 3D TI QDs based on the Faraday effect due to the Pauli exclusion principle, where the qubit is defined as either the polarization of a single e-h pair, the spin of a single electron, or the spin of a single hole. The quantum-informational methods for the implementation of quantum teleportation and quantum computing are described in Refs. 43,44. We describe here the physical methods for creating the entanglement.

A. Photon polarization - e-h pair polarization entanglement

Let us consider now the Faraday effect due to an e-h pair on the QD for the level configuration shown in Fig. 7. The initial state before the photon-QD interaction reads

$$|\psi_{\mp 1}(0)\rangle = \frac{1}{\sqrt{2}} \left(e^{-i\vartheta_0} a_{+}^{\dagger} + e^{i\vartheta_0} a_{-}^{\dagger} \right) c_{\pm}^{\dagger} v_{2\mp}^{\dagger} |0\rangle \quad (68)$$

where the photon is linearly polarized at an angle ϑ_0 from the x -axis. If the initial e-h pair is -1 polarized, then the state after time t is given by

$$\begin{aligned} |\psi_{-1}(t)\rangle &= \frac{1}{\sqrt{2}} \left(e^{-i(\vartheta_0 + \vartheta_+)} a_{+}^{\dagger}(0) + e^{i(\vartheta_0 + \vartheta_-)} a_{-}^{\dagger}(0) \right) \\ &\quad \times c_{+}^{\dagger} v_{2-}^{\dagger} |0\rangle \end{aligned} \quad (69)$$

$$\begin{aligned} &= \frac{e^{-i\left(\frac{\vartheta_+ - \vartheta_-}{2}\right)}}{\sqrt{2}} \left(e^{-i\left(\vartheta_0 + \frac{\vartheta_+ + \vartheta_-}{2}\right)} a_{+}^{\dagger}(0) \right. \\ &\quad \left. + e^{i\left(\vartheta_0 + \frac{\vartheta_+ + \vartheta_-}{2}\right)} a_{-}^{\dagger}(0) \right) c_{+}^{\dagger} v_{2-}^{\dagger} |0\rangle \end{aligned} \quad (70)$$

with $\vartheta_+(t) = -\frac{2g_2^2}{\delta} t$ and $\vartheta_-(t) = \left(\frac{2g_1^2}{\delta + \frac{\Delta_S}{\hbar}} - \frac{2g_2^2}{\delta} \right) t$, resulting in a Faraday rotation angle of $\vartheta_{-1}(t) = [\vartheta_+(t) + \vartheta_-(t)]/2 = -\left(\frac{2g_2^2}{\delta} - \frac{g_1^2}{\delta + \frac{\Delta_S}{\hbar}} \right) t$. This result is in complete agreement with the result using Fermi's golden rule above. If the initial e-h pair is $+1$ polarized, then the state after time t is given by

$$\begin{aligned} |\psi_{+1}(t)\rangle &= \frac{1}{\sqrt{2}} \left(e^{-i(\vartheta_0 + \vartheta_+(t))} a_{+}^{\dagger}(0) + e^{i(\vartheta_0 + \vartheta_-(t))} a_{-}^{\dagger}(0) \right) \\ &\quad \times c_{-}^{\dagger} v_{2+}^{\dagger} |0\rangle \end{aligned} \quad (71)$$

$$\begin{aligned} &= \frac{e^{-i\left(\frac{\vartheta_+ - \vartheta_-}{2}\right)}}{\sqrt{2}} \left(e^{-i\left(\vartheta_0 + \frac{\vartheta_+ + \vartheta_-}{2}\right)} a_{+}^{\dagger}(0) \right. \\ &\quad \left. + e^{i\left(\vartheta_0 + \frac{\vartheta_+ + \vartheta_-}{2}\right)} a_{-}^{\dagger}(0) \right) c_{-}^{\dagger} v_{2+}^{\dagger} |0\rangle \end{aligned} \quad (72)$$

with $\vartheta_+(t) = -\left(\frac{2g_1^2}{\delta + \frac{\Delta_S}{\hbar}} - \frac{2g_2^2}{\delta} \right) t$ and $\vartheta_-(t) = \frac{2g_2^2}{\delta} t$, resulting in a Faraday rotation angle of $\vartheta_{+1}(t) = [\vartheta_+(t) + \vartheta_-(t)]/2 = +\left(\frac{2g_2^2}{\delta} - \frac{g_1^2}{\delta + \frac{\Delta_S}{\hbar}} \right) t$. This result is in complete agreement with the result using Fermi's golden rule above.

In addition, the quantum-optical calculation lets us entangle the photon with the electron-hole state on the 3D TI QD. In particular, if we choose the initial state to be

$$|\psi(0)\rangle = \frac{1}{\sqrt{2}} \left(a_{+}^{\dagger} + a_{-}^{\dagger} \right) \left(c_{+}^{\dagger} v_{2-}^{\dagger} + c_{-}^{\dagger} v_{2+}^{\dagger} \right) |0\rangle \quad (73)$$

the photon and the e-h pair get fully entangled for $\vartheta_{\mp 1}(\tau) = \pm \frac{\pi}{4}$, i.e. after a time $\tau = \pi/4 \left(\frac{2g_2^2}{\delta} - \frac{g_1^2}{\delta + \frac{\Delta_S}{\hbar}} \right)$, yielding

$$\begin{aligned} |\psi(\tau)\rangle &= \frac{1}{\sqrt{2}} \left(e^{-i\frac{\pi}{4}} a_{+}^{\dagger}(0) + e^{i\frac{\pi}{4}} a_{-}^{\dagger}(0) \right) c_{+}^{\dagger} v_{2-}^{\dagger} \\ &\quad + \frac{1}{\sqrt{2}} \left(e^{-i(-\frac{\pi}{4})} a_{+}^{\dagger}(0) + e^{i(-\frac{\pi}{4})} a_{-}^{\dagger}(0) \right) c_{-}^{\dagger} v_{2+}^{\dagger} |0\rangle \end{aligned} \quad (74)$$

This state consists of a photon entangled to the e-h pair on the 3D TI QD.

We consider two possible level configurations due to the electron-hole symmetry in 3D TI QDs:

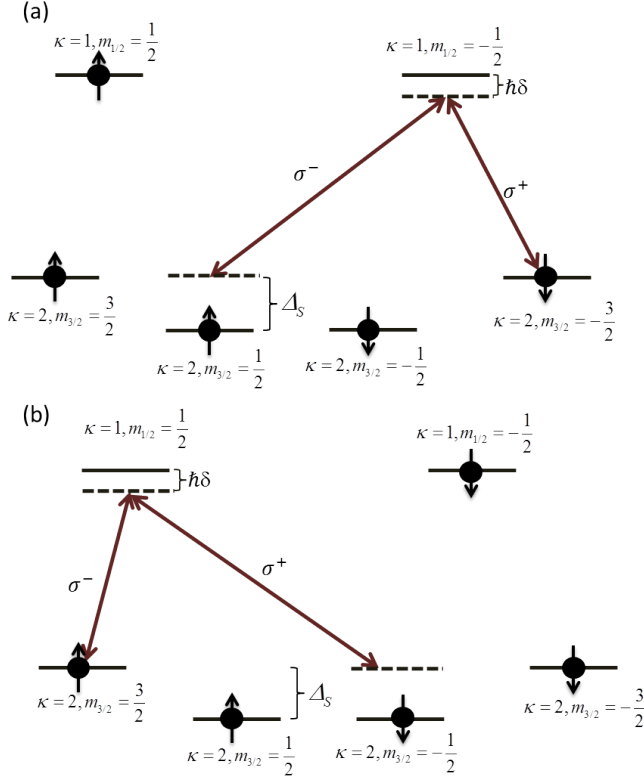


Figure 9: This is one possible level configuration that can be used for the implementation of the quantum Faraday rotation, where the quantum information is stored in form of an electron (a) in the spin up state or (b) in the spin down state. (a) A single spin up electron is probed by using off-resonant linearly polarized photon that acquires a positive Faraday rotation angle through virtual excitation of e-h pairs. (b) A single spin down electron is probed by using off-resonant linearly polarized photon that acquires a negative Faraday rotation angle through virtual excitation of e-h pairs.

1. Fig. 9 shows the first level configuration, in which only one of the states $|\Phi_{\frac{1}{2}, \pm \frac{1}{2}}^{\kappa=1}\rangle$ is populated with an electron.
2. Fig. 10 shows the second level configuration, in which only one of the states $|\Phi_{\frac{1}{2}, \pm \frac{1}{2}}^{\kappa=1}\rangle$ is populated with a hole.

B. Photon polarization - electron spin entanglement

Now let us consider the Faraday effect due to a single electron for the level configuration shown in Fig. 10. Here the electron is in a s-like state. If the initial state is

$$|\psi(0)\rangle = \frac{1}{\sqrt{2}} \left(e^{-i\vartheta_0} a_+^\dagger + e^{i\vartheta_0} a_-^\dagger \right) c_+^\dagger |0\rangle \quad (75)$$

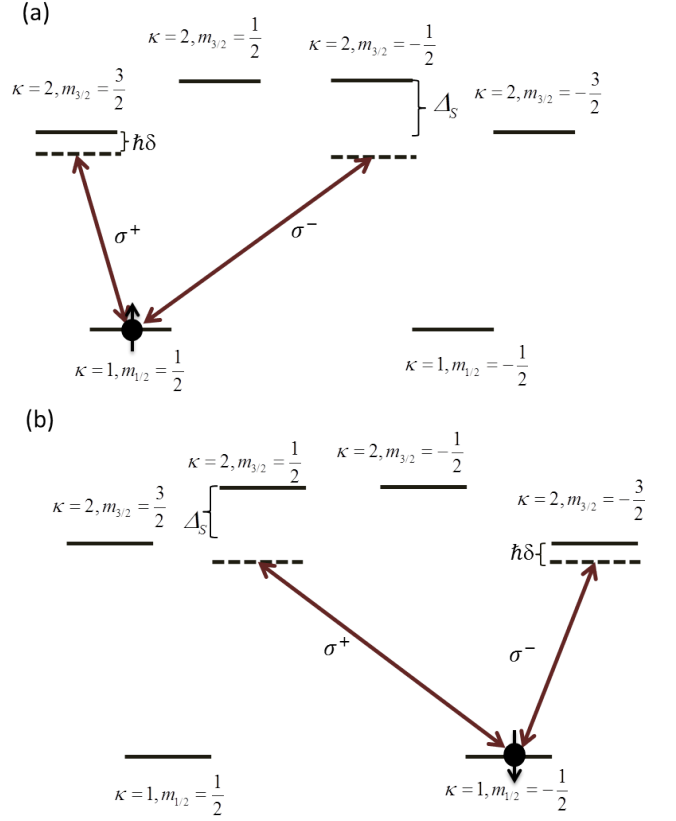


Figure 10: This is another possible level configuration that can be used for the implementation of the quantum Faraday rotation, where the quantum information is stored in form of a hole (a) in the spin up state or (b) in the spin down state. (a) A single spin up hole is probed by using off-resonant linearly polarized photon that acquires a positive Faraday rotation angle through virtual excitation of e-h pairs. (b) A single spin down hole is probed by using off-resonant linearly polarized photon that acquires a negative Faraday rotation angle through virtual excitation of e-h pairs.

then state after the interaction is given by

$$|\psi(t)\rangle = \frac{1}{\sqrt{2}} \left(e^{-i\left(\vartheta_0 - \frac{2g_2^2}{\delta}t\right)} a_+^\dagger(0) + e^{i\left(\vartheta_0 + \frac{2g_2^2}{\delta + \frac{\Delta_S}{\hbar}}t\right)} a_-^\dagger(0) \right) c_+^\dagger |0\rangle \quad (76)$$

resulting in $\vartheta_{+1}(t) = \left(\frac{g_1^2}{\delta + \frac{\Delta_S}{\hbar}} - \frac{g_2^2}{\delta} \right) t$. Conversely, if the initial state is (see Fig.10 (b))

$$|\psi(0)\rangle = \frac{1}{\sqrt{2}} \left(e^{-i\vartheta_0} a_+^\dagger + e^{i\vartheta_0} a_-^\dagger \right) c_-^\dagger |0\rangle \quad (77)$$

then state after the interaction is given by

$$|\psi(t)\rangle = \frac{1}{\sqrt{2}} \left(e^{-i\left(\vartheta_0 - \frac{2g_1^2}{\delta + \frac{\Delta_S}{\hbar}}t\right)} a_+^\dagger(0) + e^{i\left(\vartheta_0 + \frac{2g_2^2}{\delta}t\right)} a_-^\dagger(0) \right) c_-^\dagger |0\rangle \quad (78)$$

resulting in $\vartheta_{-1}(t) = -\left(\frac{g_1^2}{\delta + \frac{\Delta_S}{\hbar}} - \frac{g_2^2}{\delta}\right)t$. This result is also in complete agreement with the Faraday effect obtained above.

Again, the quantum-optical calculation allows us to entangle the photon with the single electron on the 3D TI QD. In particular, if we choose the initial state

$$|\psi(0)\rangle = \frac{1}{\sqrt{2}} (a_+^\dagger + a_-^\dagger) (c_+^\dagger + c_-^\dagger) |0\rangle \quad (79)$$

then the state after the interaction is fully entangled after a time $\tau = \pi / \left[4 \left(\frac{g_1^2}{\delta + \frac{\Delta_S}{\hbar}} - \frac{g_2^2}{\delta} \right) \right]$, i.e.

$$|\psi(\tau)\rangle = \frac{1}{\sqrt{2}} \left(e^{-i\frac{\pi}{4}} a_+^\dagger(0) + e^{i\frac{\pi}{4}} a_-^\dagger(0) \right) c_+^\dagger + \frac{1}{\sqrt{2}} \left(e^{-i(-\frac{\pi}{4})} a_+^\dagger(0) + e^{i(-\frac{\pi}{4})} a_-^\dagger(0) \right) c_-^\dagger |0\rangle \quad (80)$$

This state is a fully entangled electron-photon state.

The Faraday effect due to a single hole for the level configuration shown in Fig. 9 can be calculated in a similar way. Here the hole is in an s-like state. Other possible configurations include a single electron in a p-like state or a single hole in a p-like state.

Due to the symmetry between positive- and negative-energy solutions, in a 3D TI QD it is possible to define an electron spin qubit in terms of an s-like or a p-like state. At the same time it is possible to define a hole spin qubit in terms of an s-like or a p-like state. This cannot be done in a conventional wide-bandgap semiconductor QD, where the electron is associated with an s-like state and the hole is associated with a p-like state.⁴⁶

For a quantitative description, we can assume a single 3D TI QD embedded in a semiconductor microcavity. The strong and weak interaction can occur between the QD e-h pair and discretized cavity modes at resonance, $\omega_{21} = \omega_c$. The e-h-photon coupling parameter g is given by $g = (\pi e^2 f)^{1/2} / (4\pi\epsilon_r\epsilon_o m_o V_m)^{1/2}$, where ϵ_r is the dielectric constants for the cavity material,⁶³ m_o is the free electron mass, and V_m is the mode volume. The mode volume for a mode of wavelength λ is $V_m \approx (\lambda/2n)^3$, where $n = \sqrt{\epsilon_r}$ (for a GaAs microcavity, $n = 3.31$). Using $\hbar\omega_{21} = 130$ meV, the oscillator strengths for the transition $\Phi_{\frac{3}{2},+\frac{1}{2}}^{\kappa=2} \longleftrightarrow \Phi_{\frac{1}{2},-\frac{1}{2}}^{\kappa=1}$ and $\Phi_{\frac{3}{2},-\frac{3}{2}}^{\kappa=2} \longleftrightarrow \Phi_{\frac{1}{2},-\frac{1}{2}}^{\kappa=1}$ are obtained, respectively, $f_1 \approx 9$ and $f_2 \approx 27$. This gives us an estimate of $\hbar g_1 \approx 10$ μ eV and $\hbar g_2 \approx 17$ μ eV. For a detuning energy of $\hbar\delta = 100$ μ eV

the time it takes to fully entangle the electron spin and the photon polarization is calculated to be of the order of 180 ps. The necessary condition to be in the strong coupling regime is that g must be large compared to both spontaneous emission rate and cavity decay loss rate.⁷⁵ Thus, for $Q \geq \omega/g_1 \approx 1.3 \times 10^4$ the 3D TI QD is in the strong coupling regime. For $Q = 10^5$, the photon decay rate is given by $\kappa = \frac{\omega}{2\pi Q} = 3.1 \times 10^9$ s⁻¹. This gives a cavity photon life time of 3 ns.

IX. CONCLUSIONS

We have shown that Weyl fermions can be confined in all three dimensions at the spherically shaped interface between two narrow-bandgap semiconductor alloys, such as the core-bulk heterostructure made of PbTe/Pb_{0.31}Sn_{0.69}Te. This configuration provides us with the model of a spherical 3D TI QD with tunable size r_0 and potential Δ_0 , which allows for complete control over the number of bound interface states. The most important features of 3D TI have been identified in a 3D TI QD, namely the spin locking effect and the Kramers degeneracy. We found that the Weyl states are confined on the surface of the QD, in contrast to the electrons and holes in topologically trivial semiconductor QDs. We showed that due to the large dipole moment of 450 Debye it is possible to reach the strong-coupling regime inside a cavity with a quality factor of $Q \approx 10^4$ in the infrared wavelength regime around 10 μ m. Because of the strict optical selection rules, the 3D TI QD gives rise to interesting applications based on the semi-classical and quantum Faraday effect. We found that the 3D TI QD is a good candidate for quantum memory, quantum teleportation, and quantum computing with single spins in 3D TI QDs using infrared light. In particular, a single e-h pair, a single electron, or a single hole can be used as a qubit for the implementation of optically mediated quantum computing with 3D TI QDs. Interestingly, we found that due to the symmetry between positive- and negative-energy solutions, in a 3D TI QD it is possible to define an electron spin qubit in terms of an s-like or a p-like state. At the same time it is possible to define a hole spin qubit in terms of an s-like or a p-like state. This cannot be done in a zincblende wide direct-bandgap semiconductor QD, where the electron is associated with an s-like state and the hole is associated with a p-like state.⁴⁶

Acknowledgments

We acknowledge support from NSF (Grants ECCS-0901784 and Grant ECCS-1128597) and AFOSR (Grant FA9550-09-1-0450). M.N.L. thanks Daniel Loss for fruitful discussions during his stay at the University of Basel, Switzerland. M.N.L. acknowledges partial support

from the Swiss National Science Foundation. We thank Mikhail Erementchouk for useful discussions.

Appendix A: Calculation of the Wronskian

The Wronskian of the functions $\mathcal{I}_\kappa(z)$ and $\mathcal{K}_\kappa(z)$ is defined as⁶⁴

$$W_\kappa[\mathcal{I}_\kappa(z), \mathcal{K}_\kappa(z)] = \mathcal{I}_\kappa(z) \mathcal{K}'_\kappa(z) - \mathcal{I}'_\kappa(z) \mathcal{K}_\kappa(z), \quad (\text{A1})$$

where the prime denotes the derivative of the function. For independent solutions, it is to be noted that Wronskian is proportional to $1/p(x)$ in a Sturm-Liouville type equation $\frac{d}{dx} \left[p(x) \frac{dy}{dx} \right] + g(x)y = 0$. Therefore, Wronskians in the text are calculated to be

$$W_\kappa[\mathcal{I}_\kappa(z), \mathcal{K}_\kappa(z)] = -\frac{1}{z^2}, \quad (\text{A2})$$

$$W_{\kappa-1}[\mathcal{I}_{\kappa-1}(z), \mathcal{K}_{\kappa-1}(z)] = -\frac{1}{z^2}. \quad (\text{A3})$$

Appendix B: Limiting form of Bessel functions

The limiting forms of modified Bessel functions for $z \rightarrow 0$ are given by

$$\left. \begin{aligned} I_\kappa(z) &= \frac{1}{\Gamma(\kappa+1)} \left(\frac{z}{2}\right)^\kappa \\ K_\kappa(z) &= \frac{\Gamma(\kappa)}{2} \left(\frac{z}{2}\right)^\kappa \end{aligned} \right\} \text{ as } z \rightarrow 0. \quad (\text{B1})$$

The modified spherical Bessel functions can be written in terms of modified Bessel functions as

$$\mathcal{I}_\kappa(z) = \left(\sqrt{\frac{\pi}{2z}}\right) I_{\kappa+\frac{1}{2}}(z), \quad \mathcal{K}_\kappa(z) = \left(\sqrt{\frac{2}{\pi z}}\right) K_{\kappa+\frac{1}{2}}(z). \quad (\text{B2})$$

Therefore, the function

$$F(z) = [z\mathcal{I}_\kappa(z)\mathcal{K}_\kappa(z)][z\mathcal{I}_{\kappa-1}(z)\mathcal{K}_{\kappa-1}(z)]. \quad (\text{B3})$$

has the limiting form $F(z) = \frac{1}{4\kappa^2-1}$ as $z \rightarrow 0$.

The asymptotic expansion ($z \rightarrow \infty$) of the modified Bessel functions are given by

$$\begin{aligned} I_\kappa(z) &= \frac{e^z}{\sqrt{2\pi z}} \left\{ 1 - \frac{4\kappa^2-1}{8z} + \frac{(4\kappa^2-1)(4\kappa^2-9)}{2!(8z^2)} - \dots \right\} \\ K_\kappa(z) &= \sqrt{\frac{\pi}{2z}} e^{-z} \left\{ 1 + \frac{4\kappa^2-1}{8z} + \frac{(4\kappa^2-1)(4\kappa^2-9)}{2!(8z^2)} - \dots \right\}. \end{aligned} \quad (\text{B4})$$

Appendix C: The fermion doubling theorem

Nielsen and Ninomiya investigated Weyl fermions on a crystal.⁵² They formulated a no-go theorem, called the fermion doubling theorem, requiring that Weyl nodes in a

crystal always exist in pairs of opposite chirality. The reason for this theorem is that the number of Weyl fermions in the first Brillouin zone must be conserved. This conservation law can be checked by calculating the Berry flux in the first Brillouin zone.

It is important to note that the fermion doubling theorem is only valid for continuum states. Therefore it does not apply to the bound eigenstates of the 3D TI QD, which have a discrete eigenspectrum. Below we give arguments for the validity of the fermion doubling theorem in the continuum limit, which corresponds to the asymptotic limit when the 3D TI QD radius r_o becomes infinite.

A typical calculation of the Berry curvature $\mathcal{B}_n(\mathbf{k}) = \nabla_{\mathbf{k}} \times \mathcal{A}_n(\mathbf{k})$ considers a single band Bloch state $u_{n\mathbf{k}}(\mathbf{r})e^{i\mathbf{k}\cdot\mathbf{r}}$, which gives rise to the Berry connection $\mathcal{A}_n(\mathbf{k}) = i \int_\Omega d^3r u_{n\mathbf{k}}^*(\mathbf{r}) \nabla_{\mathbf{k}} u_{n\mathbf{k}}(\mathbf{r})$.⁶⁷ As long as the n th band does not touch or cross any other band, the Berry flux is zero, i.e. $\nabla_{\mathbf{k}} \cdot \mathcal{B}_n(\mathbf{k}) = 0$. However, if there is a band crossing, this situation changes drastically due to the monopole at the crossing point. Using $\mathbf{k} \cdot \mathbf{p}$ approximation, around the crossing point in the first Brillouin zone the Berry connection becomes $\mathcal{A}_\pm(\mathbf{k}) = i \langle \chi_\pm | \nabla_{\mathbf{k}} | \chi_\pm \rangle$, where χ_\pm is the four-spinor of the solution $\Phi_\pm = \chi_\pm F(\mathbf{r})$ of Eq. (1).⁴⁹ Assuming a very large QD, where quantum confinement can be neglected, the four-spinor reads

$$\chi_\pm = \begin{pmatrix} \pm e^{-i(\frac{\varphi \pm \pi}{2})} \\ \pm e^{i(\frac{\varphi \pm \pi}{2})} \\ e^{-i(\frac{\varphi \mp \pi}{2})} \\ e^{i(\frac{\varphi \mp \pi}{2})} \end{pmatrix} \quad (\text{C1})$$

where $e^{\mp i\varphi} = \frac{k_x \mp i k_y}{k_\perp}$ and the position-dependent function is given by $F(\mathbf{r}) = C e^{-\frac{1}{\hbar v} \int_0^z \Delta(z') dz' + i\mathbf{k}_\perp \cdot \mathbf{r}}$, where C is the normalization constant. In order to capture the Berry curvature apart from the azimuthal angle φ we need to add the dependence on the polar angle θ . At the same time, we perform the gauge transformations $e^{\pm i\varphi}$ to shift the singularity of the Berry curvature to the south pole. This means we calculate the Berry curvature with respect to the normalized 4-spinors

$$\begin{aligned} \chi_{C,+} &= \frac{1}{\sqrt{2}} \begin{pmatrix} e^{-i\frac{\pi}{4}} \cos \frac{\theta}{2} \\ e^{i(\varphi + \frac{\pi}{4})} \sin \frac{\theta}{2} \\ e^{i\frac{\pi}{4}} \cos \frac{\theta}{2} \\ e^{i(\varphi - \frac{\pi}{4})} \sin \frac{\theta}{2} \end{pmatrix}, \\ \chi_{C,-} &= \frac{1}{\sqrt{2}} \begin{pmatrix} -e^{-i(\varphi - \frac{\pi}{4})} \sin \frac{\theta}{2} \\ e^{-i\frac{\pi}{4}} \cos \frac{\theta}{2} \\ e^{-i(\varphi + \frac{\pi}{4})} \sin \frac{\theta}{2} \\ -e^{i\frac{\pi}{4}} \cos \frac{\theta}{2} \end{pmatrix} \end{aligned} \quad (\text{C2})$$

The Berry connection is then given by

$$\mathcal{A}_\pm(\mathbf{k}) = i \langle \chi_{C,\pm} | \nabla_{\mathbf{k}} | \chi_{C,\pm} \rangle = \mp \frac{(1 - \cos \theta)}{2k \sin \theta} \mathbf{e}_\varphi \quad (\text{C3})$$

where \mathbf{e}_φ is the unit vector pointing in φ -direction. Thus, we obtain the Berry phase

$$\gamma_\pm = \oint \mathcal{A}_\pm(\mathbf{k}) \cdot d\mathbf{k} = \mp\pi(1 - \cos\theta) \quad (\text{C4})$$

and the Berry curvature

$$\mathcal{B}_\pm(\mathbf{k}) = \mp \frac{1}{2k^2} \mathbf{e}_k \quad (\text{C5})$$

Note that the Berry curvature for the 4-spinor is the same as the Berry curvature of a 2-spinor.⁶⁸ For a loop on the 2D surface where $\theta = \pi/2$, we get $\gamma_\pm = \mp\pi$, which gives rise to the topological phase shift seen in Shubnikov-de Haas oscillations for the surface of 3D topological insulators.⁶⁹ From $\Delta(1/k) = \mp 4\pi\delta^{(3)}(\mathbf{k})$ and $\nabla(1/k) = \mp \frac{1}{k^2} \mathbf{e}_k$ it follows that the Berry curvature is the solution of the equation

$$\nabla_{\mathbf{k}} \cdot \mathcal{B}_\pm(\mathbf{k}) = \mp 4\pi g \delta^{(3)}(\mathbf{k}) \quad (\text{C6})$$

where $g = \mp 1/2$ is the strength of the Dirac monopole for positive and negative helicity of the 4-spinor, which is identical to the result for 2-spinors (see Refs. 68 and 70).

In order to understand the helicity of the Weyl fermions at the interface, we have shown in Ref. 49 that the helicity operator is given by

$$\hat{h}_{\text{TI}} = (1/|p_\perp|) \begin{pmatrix} (\boldsymbol{\sigma}_\perp \times \mathbf{p}_\perp) \cdot \hat{\mathbf{z}} & 0 \\ 0 & -(\boldsymbol{\sigma}_\perp \times \mathbf{p}_\perp) \cdot \hat{\mathbf{z}} \end{pmatrix} \quad (\text{C7})$$

which commutes with the Hamiltonian in Eq. (1) and yields $\hat{h}_{\text{TI}}\Phi_\pm = (\pm 1/2)\Phi_\pm$, where the + sign denotes the positive helicity of positive-energy solutions and the - sign denotes the negative helicity of negative-energy solutions. This provides the possibility to write an effective 2D Hamiltonian for the Weyl fermions on the surface of 3D topological insulators, i.e.

$$H_{2D} = \hbar v \begin{pmatrix} (\boldsymbol{\sigma}_\perp \times \mathbf{k}_\perp) \cdot \hat{\mathbf{z}} & 0 \\ 0 & -(\boldsymbol{\sigma}_\perp \times \mathbf{k}_\perp) \cdot \hat{\mathbf{z}} \end{pmatrix} \quad (\text{C8})$$

This effective 2D Hamiltonian can be reduced to two Weyl Hamiltonians of the form $H_{2D}^{2x2} = \pm \hbar v (\boldsymbol{\sigma}_\perp \times \mathbf{k}_\perp) \cdot \hat{\mathbf{z}}$. It is important to note that both 2-spinors of χ_\pm , the 2-spinor χ_\pm^{L-} of the L^- band and the 2-spinor χ_\pm^{L+} of the L^+ band have the same helicity, in contrast to the commonly used Weyl Hamiltonians $H_W(\mathbf{k}) = \pm \hbar v \boldsymbol{\sigma} \cdot \mathbf{k}$. The reason for this is that the two 2-spinors are coupled through the mass term $\Delta(z)$ in z -direction, as given in the 3D Hamiltonian in Eq. (1).

In order to satisfy the fermion doubling theorem,⁵² usually the Dirac cones on the opposite side of the slab of a 3D topological insulator are identified as the fermion

doublers. In the case of the 3D IT QD, for $r_o \rightarrow \infty$, i.e. in the continuum limit, the Berry curvature in \mathbf{k} -space for a 2D interface, given by Eq. (C5), determines

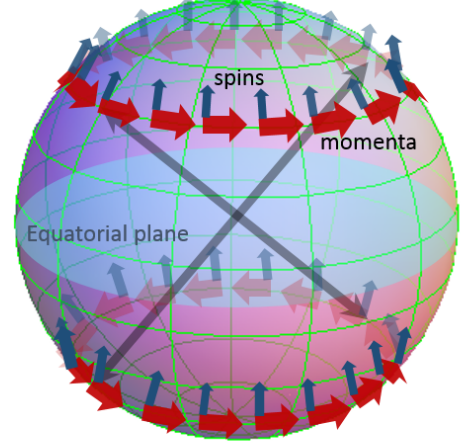


Figure 11: Two antipodal points on the surface of the sphere defined by the QD are identified as the Dirac cones of opposite helicity. One point lies on the northern hemisphere, while its antipodal point lies on the southern hemisphere. The currents flowing along the latitudes can be imagined as angular momentum states of a 3D TI QD in the continuum limit. At the antipodal points momenta (red arrows) point in opposite $\hat{\varphi}$ direction to each other while spins (blue arrows) point in the same $\hat{\theta}$ direction, where $\hat{\theta}$ and $\hat{\varphi}$ are the spherical angular unit vectors. Hence, they have opposite chirality. This satisfies the fermion doubling theorem.

the Weyl nodes that need to satisfy the fermion doubling theorem. Hence, according to Ref. 51, we can adopt the mapping of the two opposite surfaces of a 3D slab of TI onto the northern and southern hemispheres of a sphere. We then identify the pairs of Dirac cones with opposite helicity as the ones located on the antipodal points on the surface of the sphere defined by the QD, as shown in Fig. 11. Note that in both cases, the slab and the QD, the pairs of Dirac cones map into each other through the parity transformation, which in general reverses the helicity. We can identify a current on the surface of the sphere flowing along a latitude. The parity transformation then maps one latitude on the northern hemisphere with one type of helicity to its partner latitude on the southern hemisphere with the opposite helicity. These arguments show that the fermion doubling theorem is satisfied for a 3D TI QD in the continuum limit.

- * Electronic address: michael.leuenberger@ucf.edu
- ¹ Moore, J. E. The birth of topological insulators, *Nature* **464**, 194 (2010).
 - ² M. Z. Hasan and C. L. Kane, *Rev. Mod. Phys.* **82**, 3045 (2010).
 - ³ Y. L. Chen, J. G. Analytis, J.-H. Chu, Z. K. Liu, S.-K. Mo, X. L. Qi, H. J. Zhang, D. H. Lu, X. Dai, Z. Fang, S. C. Zhang, I. R. Fisher, Z. Hussain & Z.-X. Shen, *Science* **325**, 178-181 (2009).
 - ⁴ D. Hsieh, Y. Xia, L. Wray, D. Qian, A. Pal, J. H. D. J. Osterwalder, F. Meier, G. Bihlmayer, C. L. Kane, Y. S. Hor, R. J. Cava, M. Z. Hasan, *Science* **323**, 919 (2009).
 - ⁵ Y. Xia, D. Qian, D. Hsieh, L. Wray, A. Pal, H. Lin, A. Bansil, D. Grauer, Y. S. Hor, R. J. Cava, M. Z. Hasan, *Nature Phys.* **5**, 398-402 (2009).
 - ⁶ P. Roushan, J. Seo, Colin V. Parker, Y. S. Hor, D. Hsieh, Dong Qian, Anthony Richardella, M. Z. Hasan, R. J. Cava, A. Yazdani, *Nature (London)* **460**, 1106 (2009).
 - ⁷ Z. Alpichshev, J. G. Analytis, J.-H. Chu, I. R. Fisher, Y. L. Chen, Z. X. Shen, A. Fang, A. Kapitulnik, *Phys. Rev. Lett.* **104**, 016401 (2010).
 - ⁸ D. Hsieh, D. Qian, L. Wray, Y. Xia, Y. S. Hor, R. J. Cava, M. Z. Hasan, *Nature (London)* **452**, 970 (2008).
 - ⁹ H. Yusheng, A.D.C. Grassie, *J. Phys. F: Met. Phys.* **15**, 363-376 (1985).
 - ¹⁰ D. Pesin, A. H. MacDonald, *Nature Mater.* **11**, 409 (2012).
 - ¹¹ V. M. Edelstein, *Solid State Commun.* **73**, 233 (1990).
 - ¹² J. Wunderlich, B. Kaestner, J. Sinova, T. Jungwirth, *Phys. Rev. Lett.* **94**, 047204 (2005).
 - ¹³ C. L. Kane, E. J. Mele, *Phys. Rev. Lett.* **95**, 146802 (2005).
 - ¹⁴ L. Fu, C. L. Kane, *Phys. Rev. B* **76**, 045302 (2007).
 - ¹⁵ I. Zutic, J. Fabian, S. Das Sarma, *Rev. Mod. Phys.* **76**, 323-345 (2004).
 - ¹⁶ D. Hsieh, Y. Xia, D. Qian, L. Wray, J. H. Dil, F. Meier, J. Osterwalder, L. Patthey, J. G. Checkelsky, N. P. Ong, A. V. Fedorov, H. Lin, A. Bansil, D. Grauer, Y. S. Hor, R. J. Cava, M. Z. Hasan, *Nature (London)* **460**, 1101 (2009).
 - ¹⁷ L. Fu and C. L. Kane, *Phys. Rev. Lett.* **100**, 096407 (2008).
 - ¹⁸ P. J. Leek, J. M. Fink, A. Blais, R. Bianchetti, M. Göppl, J. M. Gambetta, D. I. Schuster, L. Frunzio, R. J. Schoelkopf, A. Wallraff, *Science* **318**, 1889 (2007).
 - ¹⁹ H.-T. He, G. Wang, T. Zhang, I. K. Sou, G. K. L. Wong, J. N. Wang, H. Z. Lu, S. Q. Shen, F. C. Zhang, *Phys. Rev. Lett.* **106**, 166805 (2011).
 - ²⁰ H. Peng, K. Lai, D. Kong, S. Meister, Y. Chen, X.-L. Qi, S.-C. Zhang, Z.-X. Shen, Y. Cui, *Nature Mater.* **9**, 225 (2010).
 - ²¹ J. J. Cha, K. J. Koski, Y. Cui, *Phys. Status Solidi (RRL)* **7**, 15 (2012).
 - ²² H. Peng, W. Dang, J. Cao, Y. Chen, D. Wu, W. Zheng, H. L., Z.-X. Shen, Z. Liu, *Nature Chem.* **4**, 218 (2012).
 - ²³ D. Kong, Y. Cui, *Nature Chem.* **3**, 845 (2011).
 - ²⁴ S. Cho, S. Cho, D. Kim, P. Syers, N. P. Butch, J. Paglione, M. S. Fuhrer, *Nano Lett.* **12**, 469 (2012).
 - ²⁵ C. Simon, M. Afzelius, J. Appel, A. B. de la Giroday, S. J. Dewhurst, N. Gisin, C. Y. Hu, F. Jelezko, S. Kroll, J. H. Müller, J. Nunn, E. S. Polzik, J. G. Rarity, H. De Riedmaten, W. Rosenfeld, A. J. Shields, N. Skold, R. M. Stevenson, R. Thew, I. A. Walmsley, M. C. Weber, H. Weinfurter, J. Wrachtrup, R. J. Young, *Eur. Phys. J. D* **58**, 1 (2010).
 - ²⁶ R. B. Liu, W. Yao, L. J. Sham, *Adv. Phys.* **59**, 703 (2010).
 - ²⁷ M. Kroutvar, Y. Ducommun, D. Heiss, M. Bichler, D. Schuh, G. Abstreiter, J. J. Finley, *Nature (London)* **432**, 81 (2004).
 - ²⁸ A. Ebbens, D. N. Krizhanovskii, A. I. Tartakovskii, F. Pulizzi, T. Wright, A. V. Savelyev, M. S. Skolnick, M. Hopkinson, *Phys. Rev. B* **72**, 073307 (2005).
 - ²⁹ H. J. Krenner, C. E. Pryor, J. He, P. M. Petroff, *Nano Lett.* **8**, 1750 (2008).
 - ³⁰ D. Brunner, B. D. Gerardot, P. A. Dalgarno, G. Wust, K. Karrai, N. G. Stoltz, P. M. Petroff, R. J. Warburton, *Science* **325**, 70 (2009).
 - ³¹ M. Atatüre, J. Dreiser, A. Badolato, A. Imamoglu, *Nature Physics* **3**, 101 (2007).
 - ³² A. Imamoglu, D. D. Awschalom, G. Burkard, D. P. DiVincenzo, D. Loss, M. Sherwin, A. Small, *Phys. Rev. Lett.* **83**, 4204 (1999).
 - ³³ C. Piermarocchi, P. Chen, L. J. Sham, D. G. Steel, *Phys. Rev. Lett.* **89**, 167402 (2002).
 - ³⁴ T. Calarco, A. Datta, P. Fedichev, E. Pazy, P. Zoller, *Phys. Rev. A* **68**, 012310 (2003).
 - ³⁵ M. Atatüre, J. Dreiser, A. Badolato, A. Högele, K. Karrai, A. Imamoglu, *Science* **312**, 551 (2006).
 - ³⁶ B. D. Gerardot, D. Brunner, P. A. Dalgarno, P. Ohberg, S. Seidl, M. Kroner, K. Karrai, N. G. Stoltz, P. M. Petroff, R. J. Warburton, *Nature (London)* **451**, 441 (2008).
 - ³⁷ A. N. Vamivakas, C. Y. Lu, C. Matthiesen, Y. Zhao, S. Falt, A. Badolato, M. Atatüre, *Nature (London)* **467**, 297 (2010).
 - ³⁸ A. Greilich, D. R. Yakovlev, A. Shabaev, A. L. Efros, I. A. Yugova, R. Oulton, V. Stavarache, D. Reuter, A. Wieck, M. Bayer, *Science* **313**, 341 (2006).
 - ³⁹ E. A. Stinaff, M. Scheibner, A. S. Bracker, I. V. Ponomarev, V. L. Korenev, M. E. Ware, M. F. Doty, T. L. Reinecke, D. Gammon, *Science* **311**, 636 (2006).
 - ⁴⁰ L. Robledo, J. Elzerman, G. Jundt, M. Atatüre, A. Högele, S. Fält, A. Imamoglu, *Science* **320**, 772 (2008).
 - ⁴¹ D. Kim, S. G. Carter, A. Greilich, A. S. Bracker, D. Gammon, *Nature Physics* **7**, 223 (2011).
 - ⁴² A. N. Vamivakas, Y. Zhao, C. Y. Lu, M. Atatüre, *Nature Physics* **5**, 198 (2009).
 - ⁴³ M. N. Leuenberger, M. E. Flatté, D. D. Awschalom, *Phys. Rev. Lett.* **94**, 107401 (2005).
 - ⁴⁴ M. N. Leuenberger, *Phys. Rev. B* **73**, 075312 (2006).
 - ⁴⁵ C. Y. Hu, A. Young, J. L. O'Brien, W. J. Munro, J. G. Rarity, *Phys. Rev. B* **78**, 085307 (2008).
 - ⁴⁶ J. Singh, *Electronic and Optoelectronic Properties of Semiconductor Structures* (Cambridge University Press, Cambridge, 2003).
 - ⁴⁷ G. Nimtz, B. Schlicht, in *Narrow Gap Semiconductors* (Springer, Berlin, 1983), pp. 45-48.
 - ⁴⁸ J. J. Sakurai, *Advanced Quantum Mechanics* (Pearson Education, 2007).
 - ⁴⁹ H. P. Paudel and M. N. Leuenberger, preprint: <http://arxiv.org/abs/1208.4806>.
 - ⁵⁰ B. A. Volkov and Pankratov, *JETP Lett.* **42**, 178 (1985).
 - ⁵¹ D.-H. Lee, *Phys. Rev. Lett.* **103**, 196804 (2009).
 - ⁵² H. B. Nielsen and M. Ninomiya, *Phys. Lett. B* **130**, 389 (1983); *Nuclear Phys. B* **185**, 20 (1981); *Nuclear Phys. B* **193**, 173 (1981); *Phys. Lett. B* **105**, 219 (1981).
 - ⁵³ G. Bastard, *Wave Mechanics Applied to Semiconductor Heterostructures* (Wiley, New York, 1991).

- ⁵⁴ E. Rosencher, B. Vinter, *Optoelectronics*, (Cambridge University Press, Cambridge, 2004).
- ⁵⁵ H. P. Seigneur, G. González, Michael N. Leuenberger, W. V. Schoenfeld, *Adv. OptoElectronics* **2011**, 893086 (2011).
- ⁵⁶ G. González, H. P. Seigneur, W. V. Schoenfeld, Michael N. Leuenberger, *J. Comput. Theor. Nanosci.* **7**, 1651 (2010).
- ⁵⁷ H. P. Seigneur, G. González, Michael N. Leuenberger, W. V. Schoenfeld, *Adv. Math. Phys.* **2010**, 342915 (2010).
- ⁵⁸ A. V. Thompson, H. P. Seigneur, Michael N. Leuenberger, W. V. Schoenfeld, *IEEE J. of Quantum Electronics* **45**, 637 (2009).
- ⁵⁹ H. P. Seigneur, Michael N. Leuenberger, W. V. Schoenfeld, *J. Appl. Phys.* **104**, 014307 (2008).
- ⁶⁰ J. Berezovsky, M. H. Mikkelsen, O. Gywat, N. G. Stoltz, L. A. Coldren & D. D. Awschalom, *Science* **314**, 1916 (2006).
- ⁶¹ J. H. Davies, *The Physics of Low-dimensional Semiconductors: An Introduction* (Cambridge University Press, New York, 1997).
- ⁶² M. O. Scully, M. S. Zubairy, *Quantum Optics* (Cambridge Univ. Press, Cambridge, 2001).
- ⁶³ J. P. Reithmaier, G. Sek, A. Löffler, C. Hofmann, S. Kuhn, S. Reitzenstein, L. V. Keldysh, V. D. Kulakovskii, T. L. Reinecke, A. Forchel, *Nature (London)* **432**, 197 (2004).
- ⁶⁴ M. Abramowitz, I. A. Stegun, *Handbook of mathematical functions*, p. 443 (Natl. Bur. Std., Washington, 1972).
- ⁶⁵ T. H. Stievater, X. Li, D. G. Steel, D. Gammon, D. S. Katzer, D. Park, C. Piermarocchi, L. J. Sham, *Phys. Rev. Lett.* **87**, 133603 (2001).
- ⁶⁶ T. Takagahara, *Quantum Coherence, Correlation and Decoherence in Semiconductor Nanostructures* (Academic Press, San Diego, 2003).
- ⁶⁷ M. P. Marder, *Condensed Matter Physics* (2nd edition, Wiley, New York, 2010).
- ⁶⁸ R. Shankar, *Principles of Quantum Mechanics* (2nd edition, Springer, Berlin, 1994).
- ⁶⁹ M. Veldhorst, M. Snelder, M. Hoek, T. Gang, V. K. Guduru, X. L. Wang, U. Zeitler, W. G. van der Wiel, A. A. Golubov, H. Hilgkamp, A. Brinkman, *Nature Mat.* **11**, 417 (2012).
- ⁷⁰ M. Nakahara, *Geometry, Topology, and Physics* (2nd edition, Institute of Physics Publishing, Bristol, 2003).
- ⁷¹ J. C. Y. Teo, L. Fu, C. L. Kane, *Phys. Rev. B* **78**, 045426 (2008).
- ⁷² J. J. Sakurai, *Modern Quantum Mechanics* (Addison-Wesley, New York, 1994).
- ⁷³ S.-Y. Xu, C. Liu, N. Alidoust, M. Neupane, D. Qian, I. Belopolski, J. D. Denlinger, Y. J. Wang, H. Lin, L. A. Wray, G. Landolt, B. Slomski, J. H. Dil, A. Marcinkova, E. Morosan, Q. Gibson, R. Sankar, F. C. Chou, R. J. Cava, A. Bansil, M. Z. Hasan, *Nature Comm.* **3**, 1192 (2012).
- ⁷⁴ P. Y. Yu and M. Cardona, *Fundamentals of Semiconductors: Physics and Material Properties* (3rd edition, Springer, Berlin, 2005).
- ⁷⁵ M. Fox, *Quantum Optics: An Introduction* (Oxford University Press, 2006).